












GDAP1 loss of function inhibits the mitochondrial pyruvate dehydrogenase complex by altering the actin cytoskeleton

Christina Wolf¹, Alireza Pouya ¹, Sara Bitar¹, Annika Pfeiffer ¹, Diones Bueno ¹, Liliana Rojas-Charry¹, Sabine Arndt ², David Gomez-Zepeda², Stefan Tenzer ², Federica Dal Bello^{1,3,4}, Caterina Vianello ^{1,3,4}, Sandra Ritz⁵, Jonas Schwirz⁵, Kristina Dobrindt⁶, Michael Peitz ^{6,7}, Eva-Maria Hanschmann⁸, Pauline Mencke⁹, Ibrahim Boussaad ^{9,10}, Marion Silies ¹¹, Oliver Brüstle⁶, Marta Giacomello ^{3,4}, Rejko Krüger^{9,12} & Axel Methner ¹✉

Charcot-Marie-Tooth (CMT) disease 4A is an autosomal-recessive polyneuropathy caused by mutations of ganglioside-induced differentiation-associated protein 1 (GDAP1), a putative glutathione transferase, which affects mitochondrial shape and alters cellular Ca²⁺ homeostasis. Here, we identify the underlying mechanism. We found that patient-derived motoneurons and *GDAP1* knockdown SH-SY5Y cells display two phenotypes: more tubular mitochondria and a metabolism characterized by glutamine dependence and fewer cytosolic lipid droplets. GDAP1 interacts with the actin-depolymerizing protein Cofilin-1 and beta-tubulin in a redox-dependent manner, suggesting a role for actin signaling. Consistently, GDAP1 loss causes less F-actin close to mitochondria, which restricts mitochondrial localization of the fission factor dynamin-related protein 1, instigating tubularity. GDAP1 silencing also disrupts mitochondria-ER contact sites. These changes result in lower mitochondrial Ca²⁺ levels and inhibition of the pyruvate dehydrogenase complex, explaining the metabolic changes upon GDAP1 loss of function. Together, our findings reconcile GDAP1-associated phenotypes and implicate disrupted actin signaling in CMT4A pathophysiology.

¹Institute of Molecular Medicine, University Medical Center Mainz, Mainz, Germany. ²Institute for Immunology, University Medical Center Mainz, Mainz, Germany. ³Department of Biology, University of Padova, Padova, Italy. ⁴Department of Biomedical Sciences, University of Padova, Padova, Italy. ⁵Institute of Molecular Biology (IMB) gGmbH, Mainz, Germany. ⁶Institute of Reconstructive Neurobiology, University of Bonn Medical Faculty and University Hospital Bonn, Bonn, Germany. ⁷Cell Programming Core Facility, University of Bonn School of Medicine, Bonn, Germany. ⁸Department of Neurology, Medical Faculty, Heinrich-Heine University, Düsseldorf, Germany. ⁹Translational Neuroscience, Luxembourg Centre for Systems Biomedicine (LCSB), University of Luxembourg, Belvaux, Luxembourg. ¹⁰Disease Modeling and Screening Platform (DMSP), Luxembourg Centre of Systems Biomedicine (Biomedicine), University of Luxembourg and Luxembourg Institute of Health (LIH), Belvaux, Luxembourg. ¹¹Institute of Development Biology and Neurobiology, Johannes Gutenberg-University Mainz, Mainz, Germany. ¹²Transversal Translational Medicine, Luxembourg Institute of Health (LIH), Strassen, Luxembourg. ✉email: axel.methner@gmail.com

Charcot-Marie-Tooth (CMT) disease is the most frequently inherited peripheral neuropathy in humans and affects one in 2500 people. Clinically, this group of diseases can be distinguished by mode of inheritance, age of onset, and by electrophysiological characteristics that distinguish demyelinating and axonal forms. Mutations in the gene *GDAP1* (ganglioside-induced differentiation-associated protein 1) cause various forms of CMT: the most frequent recessively inherited demyelinating subtype CMT4A¹, the axonal-recessive (AR)-CMT2², the intermediate-recessive subtype CMTRIA³, and the dominant subtype CMT2K⁴.

GDAP1 is located in the mitochondrial outer membrane facing the cytosol. It possesses two glutathione transferase (GST)-like domains^{2,5,6} and a C-terminal hydrophobic anchor which crosses the outer mitochondrial membrane⁷. Whether *GDAP1* is a catalytically active GST remains controversial^{6,8–10}, but it appears clear that *GDAP1* can bind GST substrates^{9,10}.

One potential mechanism of *GDAP1* action that has been connected to CMT4A disease is mitochondrial dynamics. Over-expression of *GDAP1*, but not over-expression of *GDAP1* bearing recessive disease-causing mutations, results in more fragmented mitochondria, whereas a *GDAP1* knockdown (KD) results in mitochondrial elongation¹¹. This *GDAP1*-mediated mitochondrial fragmentation depends on the activity of dynamin-related protein 1 (DRP1), the major mitochondrial fission factor^{12,13}. The mechanism behind this is unknown. DRP1 is a cytosolic protein which, when recruited to mitochondria, promotes fission by forming ring-like oligomers that constrict and divide mitochondria¹⁴. The recruitment of DRP1 to mitochondria depends on the presence of ER tubules¹⁵ and filamentous actin (F-actin)¹⁶ at the sites of constriction. The ER-protein inverted formin 2 (INF2) promotes actin polymerization which occurs before DRP1-driven constriction¹⁷. INF2-mediated actin polymerization also increases mitochondria-ER contact sites (MERCs)¹⁸. This further connects actin polymerization and *GDAP1* function as mitochondrial and ER marker proteins colocalize less frequently in *GDAP1* KD cells¹⁹. Interestingly, INF2 mutations also cause CMT disease (CMTDIE)²⁰, implying that actin polymerization is important for the survival of peripheral nervous system neurons, similar to *GDAP1* function. Another protein at the interface of F-actin polymerization and DRP1 recruitment is Cofilin-1. Cofilin-1 binds to monomeric actin and F-actin and controls cytoskeletal dynamics mostly by actin depolymerization. Cofilin-1 deletion results in DRP1 accumulation at mitochondria and fragmentation²¹. In summary, defective actin polymerization affects the same mitochondrial fission pathway upstream of DRP1 and results in a clinical phenotype similar to *GDAP1* mutation. Whether F-actin polymerization and its regulation play a role in CMT4A is still poorly understood.

Another process that is affected by loss of *GDAP1* is cellular Ca^{2+} homeostasis. Neuronal *GDAP1* KD reduces Ca^{2+} influx from the extracellular space that follows depletion of the ER Ca^{2+} stores, so-called store-operated Ca^{2+} entry (SOCE), possibly due to an impaired mitochondrial localization at subplasmalemmal microdomains¹⁹. *GDAP1* KD also blunts the Ca^{2+} -dependent increase of mitochondrial respiration upon SOCE²². Mitochondrial Ca^{2+} levels increase the activity of several enzymes of the tricarboxylic acid cycle (TCA) like pyruvate dehydrogenase (PDH)²³, the key enzyme of the pyruvate dehydrogenase complex (PDC) which catalyzes the conversion of pyruvate to acetyl-CoA and links glycolysis to the TCA. This connection between Ca^{2+} and TCA activity is thought to connect mitochondrial activity to ATP demand. Changes in the activity of the PDC have not been studied yet in CMT4A or in cells with perturbed *GDAP1* expression but, interestingly, a pathogenic mutation of pyruvate dehydrogenase kinase isoenzyme 3 (PDK3) that inhibits the PDC also causes CMT disease, CMTX6²⁴. How *GDAP1*-mediated

changes of the mitochondrial Ca^{2+} homeostasis are connected to its fission activity is still unclear.

In this study, we used motoneurons obtained from CMT4A-patient-derived induced-pluripotent stem cells and neuronal *GDAP1* KD cells to study the pathophysiology of CMT4A. We found that *GDAP1* interacts with actin-binding Cofilin-1. Loss of *GDAP1* results in a reduction of F-actin fibers in mitochondrial proximity, which restricts DRP1 access to mitochondrial constriction sites and disrupts mitochondria-ER contact sites. This reduces mitochondrial Ca^{2+} levels and inhibits the PDC resulting in a rewired cellular metabolism characterized by glutamine dependence and increased consumption of fatty acids. Together, these findings implicate disrupted F-actin signaling in CMT4A pathophysiology.

Results

More tubular mitochondria and an increased mitochondrial membrane potential in CMT4A patient-derived neuronal cells and *GDAP1* knockdown cells. To establish a model for CMT4A, we compared *GDAP1* KD SH-SY5Y cells^{19,25} with neuronal cells derived from CMT4A patients. Patient CMT#1 is a 25-year-old ambulant male with a compound heterozygosity (L239F/R273G) of mutations in the C-terminal GST domain of *GDAP1* and patient CMT#2 is a 40-year-old wheelchair-bound male with a homozygous mutation of the intron 4 splice donor site (c.579 + 1G>A). This mutation causes skipping of exon 4 leading to a frameshift and a truncated protein lacking the C-terminal GST and the transmembrane domain of *GDAP1* (Fig. 1a).

We generated induced-pluripotent stem cells from fibroblast cell lines²⁶ from these patients using non-integrative expression of the Yamanaka factors and differentiated them to neuronal precursor cells (NPCs) (Fig. 1b) that express the neuronal marker protein β -III tubulin (Fig. 1c). In contrast to fibroblasts²⁶, control and CMT#1 NPCs express *GDAP1* detectable by immunoblotting (Fig. 1d). NPCs from CMT#2 lacked *GDAP1* expression (Fig. 1d). Because the polyclonal antiserum targets an antigen which should still be present in the patient, this is probably due to nonsense-mediated mRNA decay or degradation of the truncated protein.

We quantified mitochondrial shape and membrane potential ($\Delta\psi_m$) using automated high-content confocal microscopy analysis of cells simultaneously stained with the fluorescent dyes mitotracker and tetramethylrhodamine methyl ester (TMRM). Patient-derived neuronal cells contained significantly more tubular mitochondria (Fig. 1e) with a more negative mitochondrial membrane potential (Fig. 1f). Applying the same methodology to *GDAP1* KD cells (Fig. 1g), we found similar changes; more elongated mitochondria (Fig. 1h) and a significantly more negative membrane potential (Fig. 1i). The consistency between the phenotypes of patient-derived cells and *GDAP1* KD cells suggests that *GDAP1* KD cells are a suitable model to study CMT4A disease.

***GDAP1* knockdown uncouples mitochondrial respiration from ATP generation.** Mitochondria produce ATP by consuming oxygen and the energetic electron donors NADH and FADH_2 in a process called oxidative phosphorylation. NADH is provided by the TCA, PDH and β -oxidation. To assess the effect of *GDAP1* KD on this all-important process, we measured mitochondrial oxygen consumption using high-resolution respirometry and found a higher mitochondrial routine respiration in *GDAP1* KD cells (Fig. 2a). The maximal capacity of the electron transfer system (ETS), determined by titrating in the uncoupler FCCP, was however similar in both cell lines (Fig. 2a). Normalization of the respiratory states to the maximum ETS capacity, the so-called flux control ratio, revealed that the *GDAP1* KD cells use a higher

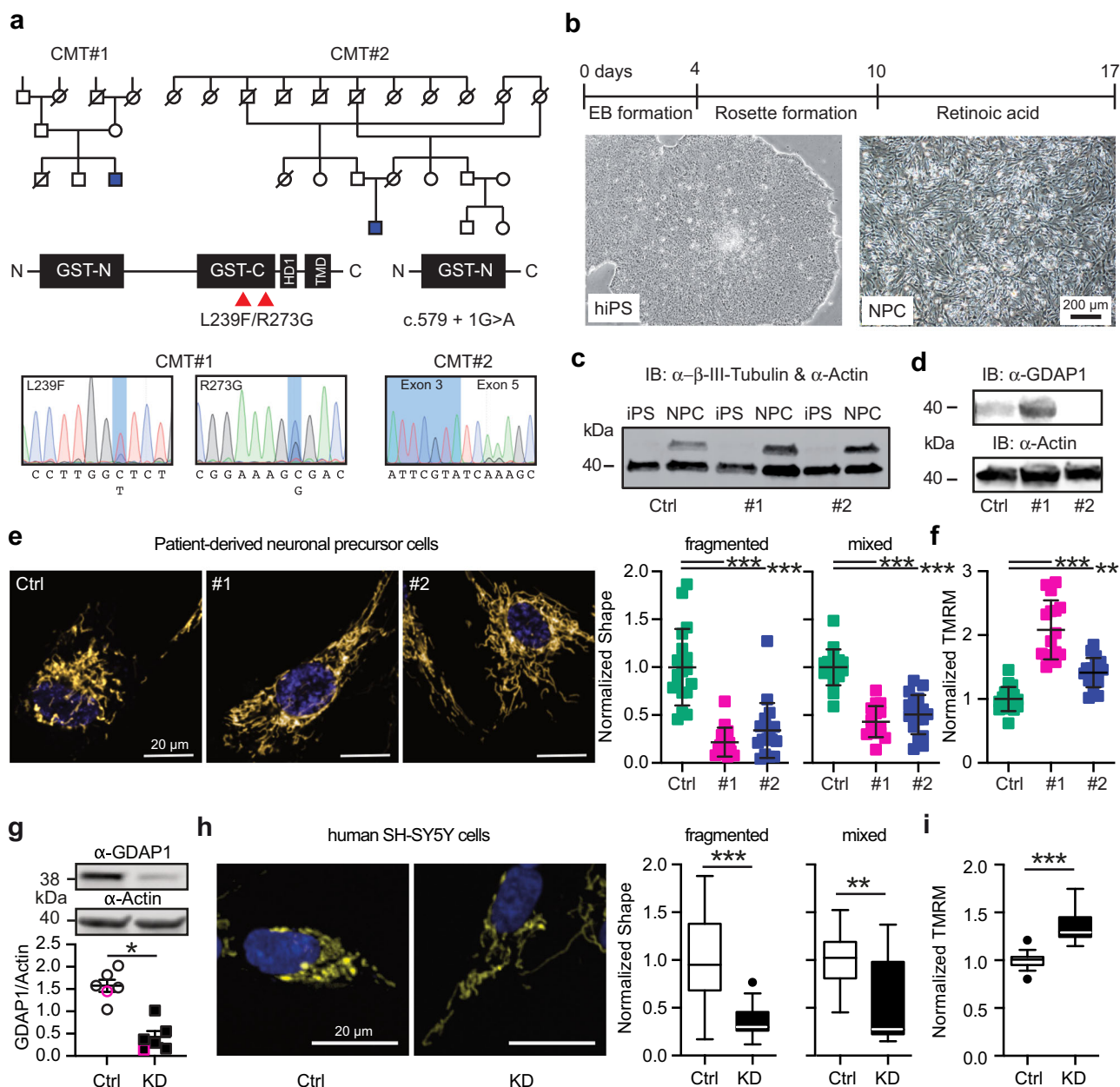


Fig. 1 More tubular mitochondria and an increased mitochondrial membrane potential in CMT4A patient-derived neuronal cells and GDAP1 knockdown cells. **a** Pedigree and GDAP1 DNA sequences from two patients suffering from autosomal-recessive CMT4A disease. **b** Differentiation protocol to obtain neuronal precursor cells from induced-pluripotent stem cells (iPSCs). **c** Immunoblot demonstrating expression of the neuronal marker β -tubulin III in the NPCs but not in iPSCs. **d** Control and CMT#1 but not CMT#2 neuronal cells express GDAP1 shown by immunoblotting. Size is indicated, Actin served as loading control. **e, h** Representative images of automated high-content confocal microscopy analysis of mitochondrial shape (MitoTracker) in patient-derived (**e**) and *GDAP1* KD (**h**) cells demonstrating elongated mitochondria in *GDAP1* loss-of-function cells. **f, i** Increased mitochondrial membrane potential (TMRM) in patient-derived (**f**) and *GDAP1* KD (**i**) cells. The values obtained in control cells were set as 1. **g** GDAP1 immunoblot and quantification demonstrating successful knockdown. Size is indicated, Actin served as loading control. Data in **e** and **f** are from 3 independent experiments with 4–8 replicates per experiment with a range of 74 to 1908 cells per well. Data in (**h**) and (**i**) are from 4 independent experiments with 4–8 replicates with a range of 343 to 4977 cells per well. Statistical variation is shown as scatter plot (**e–g**) or Tukey boxplot (**h, i**) and significance calculated using one-way ANOVA (**e, f**) or Mann-Whitney (**g–i**) tests, * $p < 0.05$, ** $p < 0.001$, *** $p < 0.0001$.

fraction of their maximal capacity for routine, leak and phosphorylating respiration (Fig. 2a'). An increased ratio between non-phosphorylating leak respiration (electron flow coupled to proton pumping to compensate for proton leaks) and ETS capacity suggests intrinsic uncoupling or dysfunction in *GDAP1* KD cells. Quantification of ATP content using the ratiometric reporters BTeam targeted either to the cytosol or to the mitochondrial matrix²⁷ also demonstrated a reduced mitochondrial ATP

generation in *GDAP1* KD cells despite the increased $\Delta\psi_m$ and routine respiration (Fig. 2b). Taken together, these data suggest that *GDAP1* KD results in the uncoupling of mitochondrial respiration and ATP generation via oxidative phosphorylation.

GDAP1 knockdown shifts cellular metabolism towards glutaminolysis. To identify metabolic pathways in *GDAP1* KD cells

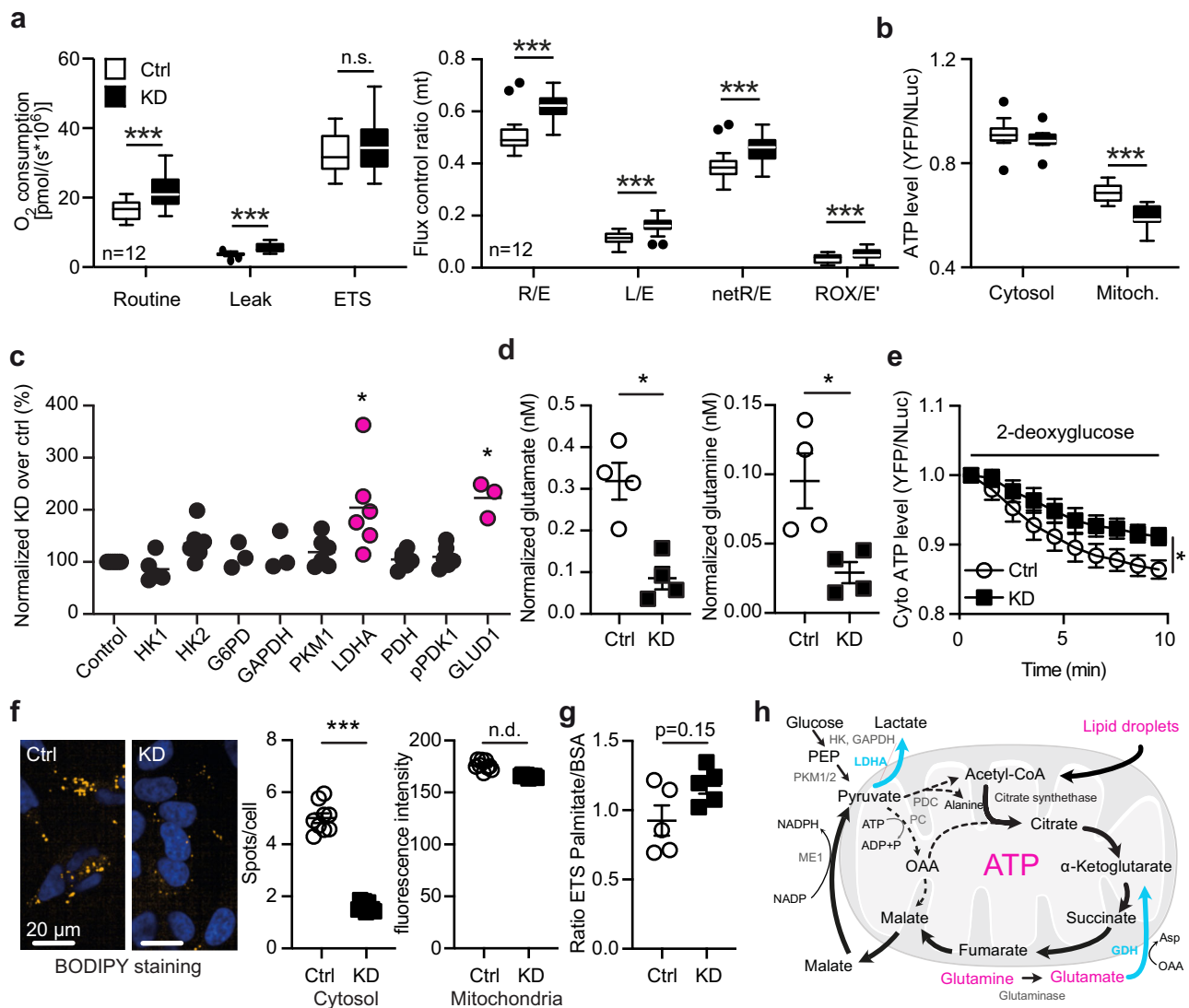


Fig. 2 *GDAP1* knockdown uncouples mitochondrial respiration from ATP generation and shifts metabolism towards glutaminolysis. **a** Mitochondrial oxygen consumption of intact cells in regular growth medium measured by high-resolution respirometry and corrected for ROX. ETS, electron transfer system; L, leak respiration; R, routine respiration; E, ETS capacity; ROX, residual oxygen consumption; netR, oxygen consumption minus ROX. Calculation of flux control ratios. **b** Comparison of cytosolic and mitochondrial ATP content using the genetically encoded ATP sensor BTeam. Calculation of BTeam YFP/NLuc emission ratios under basal conditions revealed reduced mitochondrial ATP levels. **c** Immunoblot quantification of proteins involved in glycolysis in Ctrl and KD cells shows an increase in lactate dehydrogenase A (LDHA) and glutamate dehydrogenase 1 (GLUD1) levels. HK, Hexokinase; G6PD, glucose-6-phosphate dehydrogenase; GAPDH, Glyceraldehyde 3-phosphate dehydrogenase; PKM1, pyruvate kinase M1; PDH, pyruvate dehydrogenase; pPKD1, phospho-pyruvate dehydrogenase kinase. Actin expression served as loading control. **d** Diminished glutamate and glutamine levels determined by a luminescence-based assay. **e** Comparison of cytosolic ATP content using the genetically encoded ATP sensor BTeam. BTeam YFP/NLuc emission ratios after treatment with 25 μ M 2-deoxyglucose reveals increased non-glucose dependent ATP generation capacity in KD cells. **f** Automated high-content confocal microscopy analysis of BODIPY-stained fatty acids demonstrating less lipid droplets in KD cells identified by Höchst staining of nuclei. Lipid droplets close to mitochondria were identified by MitoTracker staining. **g** ETS capacity in the presence of palmitate or BSA as substrates measured by high-resolution respirometry. **h** Schematic illustration of metabolic changes observed in *GDAP1* KD cells. Upregulation is shown in blue and bold lines; downregulation in magenta and dashed lines. ME, malic enzyme 1; PDC, pyruvate dehydrogenase complex; PKM1/2, pyruvate kinase M1/2; OAA, oxaloacetate. Data in (**a**) and (**a'**) are from 12 independent experiments performed in duplicate. Data in (**b**) are from 4 independent experiments performed in triplicates. Data in (**e**) are from 6 independent experiments performed in triplicates. Data in (**f**) were from >10,000 cells in total and were analyzed in 3 independent experiments performed in triplicates. Statistical variation is shown as Tukey's boxplots in (**a**) and (**b**), XY graph in (**c**), scatter plots in (**d**) and (**f**), mean \pm SEM in (**e**). Significance was calculated using the student's *t* test in (**a**), 2-way ANOVA in **b**, the non-parametric Kruskal-Wallis test in (**c**), the Mann-Whitney test in (**d-g**), **p* < 0.05, ***p* < 0.001, ****p* < 0.0001.

that compensate for the diminished capacity for oxidative phosphorylation, we quantified the expression levels of various metabolic enzymes in control and KD cells by immunoblotting. This revealed a significant higher protein levels of lactate dehydrogenase (LDHA) and glutamate dehydrogenase 1 (GLUD1) in

GDAP1 KD cells (Fig. 2c, Supplementary Fig. 1). LDHA catalyzes the interconversion of pyruvate to lactate. GLUD1, in contrast, converts glutamate to α -ketoglutarate, the precursor of succinyl-CoA in the TCA. In line with the increased expression of GLUD1, *GDAP1* KD cells consume significantly more glutamate, the

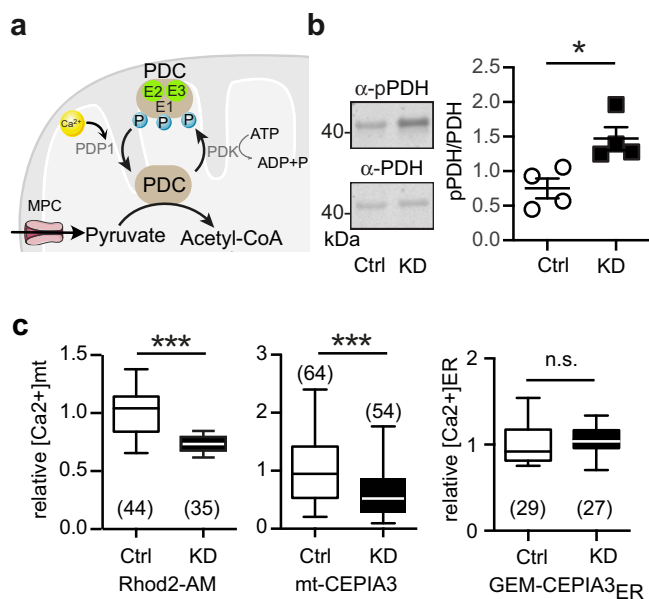


Fig. 3 Hyperphosphorylated pyruvate dehydrogenase and reduced mitochondrial Ca²⁺ levels in *GDAP1* KD cells. **a** Scheme showing the regulation of the pyruvate dehydrogenase complex (PDC). The PDC E1 subunit can be phosphorylated by the catalytic activity of the PDH kinase (PDK). The PDH phosphatase subunit 1 (PDP1) in turn dephosphorylates the serine residues upon activation by Ca²⁺. MPC, mitochondrial pyruvate carrier; PDK1, pyruvate dehydrogenase kinase 1. **b** Immunoblots from whole cell lysates for quantification of PDH E1 phosphorylation (serine 293), normalized to total PDH E1 levels revealed increased phosphorylation of PDH in *GDAP1* KD cells. **c** Mitochondrial Ca²⁺ measured with the fluorescent dye Rhod2-AM or mito-CEPIA normalized to mito-FarRed indicated reduced mt[Ca²⁺] levels. ER[Ca²⁺] levels measured with the genetically encoded Ca²⁺ sensor GEM-CEPIA3_{ER} did not show any variation between the cell lines. Data in **(c)** were from 3 independent experiments with the indicated number of cells. Data for GEM-CEPIA3_{ER} were from 2 independent experiments. Statistical variation is shown as scatter plots in **(b)** and Tukey boxplots in **(c)**. Significance was calculated using the non-parametric Mann-Whitney in **(b)** and Student's *t* test in **(c)**, **p* < 0.05, ***p* < 0.001, ****p* < 0.0001.

substrate of GLUD1, and more glutamine which can be converted to glutamate by glutaminase (Fig. 2d). We also observed an attenuated decline in cytosolic ATP content in KD cells after treatment with the glucose antimetabolite 2-deoxyglucose (Fig. 2e) in line with a reduced use of glucose as the major fuel for the TCA cycle. The TCA metabolite upstream of α-ketoglutarate is citrate, which is produced by the transfer of acetyl-CoA to oxaloacetate. Acetyl-CoA is the product of the PDC in the mitochondrial matrix or of mitochondrial β-oxidation. We suspected a dysfunction of the TCA cycle in *GDAP1* KD cells at the level of the PDC and therefore quantified the amount of lipid droplets as alternative sources for acetyl-CoA via β-oxidation in *GDAP1* KD cells. We quantified the amount of lipid droplets by BODIPY C₁₂ staining and indeed found decreased cytosolic lipid droplet levels in *GDAP1* KD cells, whereas lipid droplets associated with mitochondria were unchanged (Fig. 2f). Maximum oxygen consumption of *GDAP1* KD cells indeed tended to be higher in the presence of the fatty acid oxidation substrate palmitate (Fig. 2g). Together, these results are in line with a high lipid catabolism that serves to replenish fatty acids and consequently acetyl-CoA levels in the TCA cycle. We posit that the increased demand of glutamine and fatty acids in *GDAP1* KD probably serve as compensatory

mechanisms, clearly pointing towards a dysfunction of the TCA cycle in *GDAP1* KD cells at the level of the PDC (summarized in Fig. 2h).

Hyperphosphorylated pyruvate dehydrogenase and reduced mitochondrial Ca²⁺ levels in *GDAP1* KD cells. Increased mitochondrial Ca²⁺ levels activate the PDC by stimulating PDH phosphatase²⁸. Ca²⁺ also activates isocitrate dehydrogenase which is upstream of α-ketoglutarate, the product of GLUD1, and α-ketoglutarate dehydrogenase²⁹. Based on the reported attenuated mitochondrial respiration upon SOCE in *GDAP1* KD cells²², we suspected altered PDH phosphorylation levels driven by changes in mitochondrial Ca²⁺ content as the reason for PDC inhibition (see scheme in Fig. 3a). To test this idea, we probed phosphorylation of serine 293 of the E1 PDH subunit, which has been directly linked to PDC activity³⁰. Immunoblotting showed a significantly increased phosphorylation of PDH E1 serine 293 in *GDAP1* KD cells as compared to total E1 PDH (Fig. 3b). This is in line with a decreased activity of the PDC. We then measured mitochondrial Ca²⁺ levels by imaging live cells stained with Rhod2-AM or expressing the genetically encoded mitochondrial Ca²⁺ sensor mito-CEPIA³¹ normalized to mito-FarRed. The Ca²⁺ sensor GEM-CEPIA1er targeted to the ER served as a control. Both methods revealed a reduction in steady-state mitochondrial Ca²⁺ levels in *GDAP1* KD cells, whereas ER calcium levels were not affected (Fig. 3c). We conclude that the PDC malfunction in *GDAP1* KD cells is likely caused by a reduction in mitochondrial Ca²⁺ levels resulting in an increased phosphorylation of PDH.

Patient-derived cells are similarly characterized by increased glutaminolysis, reduced lipid droplets and reduced mitochondrial Ca²⁺ levels. We next tested whether the findings of reduced mitochondrial Ca²⁺ levels and increased glutaminolysis also apply to patient-derived cells. We set out to specifically test this in motoneurons, a cell type affected by CMT4A. Motoneurons were differentiated from NPCs following established protocols (Fig. 4a) and motoneuronal identity was confirmed by immunostaining against the dendrite marker MAP2 and the motoneuronal neurofilament H marker antibody Smi32 (Fig. 4b). Control and patient-derived motoneurons stained similarly for these markers as shown by high-content imaging (Supplementary Fig. 2). These motoneurons express *GDAP1* similar to NPCs with cells from patient CMT#2 lacking *GDAP1* expression (Fig. 4c). High-content microscopy of MitoTracker-stained cells revealed an increased area occupied by mitochondria (Fig. 4d). Immunoblotting reproduced the increased expression of GLUD1 seen upon *GDAP1* KD (Figs. 4e, 2c). Motoneurons differentiated from patient-derived cells also increased the consumption of the GLUD1-substrate glutamate (Figs. 4f, 2d) and its precursor glutamine. Furthermore, motoneurons showed a decrease in lipid droplets normalized to the nuclear area (Fig. 4g), indicative of increased fatty acid consumption. Together, these data further highlight the similarity between patient-derived cells and *GDAP1* KD cells.

Because motoneuronal cells showed a low transfection efficiency which made it difficult to identify single neurons in the cultures, we reverted to the patient-derived NPCs instead of fully differentiated motoneurons to assess the mitochondrial Ca²⁺ phenotype. We measured lower resting Ca²⁺ levels with Rhod2-AM and mito-CEPIA (Fig. 4h) in NPCs, similar to KD cells. Patient-derived NPCs also had increased levels of pPDH as compared to total PDH levels (Fig. 4i). We conclude that neuronal cells from patients with *GDAP1* mutation not only have the same changes in mitochondrial shape and membrane

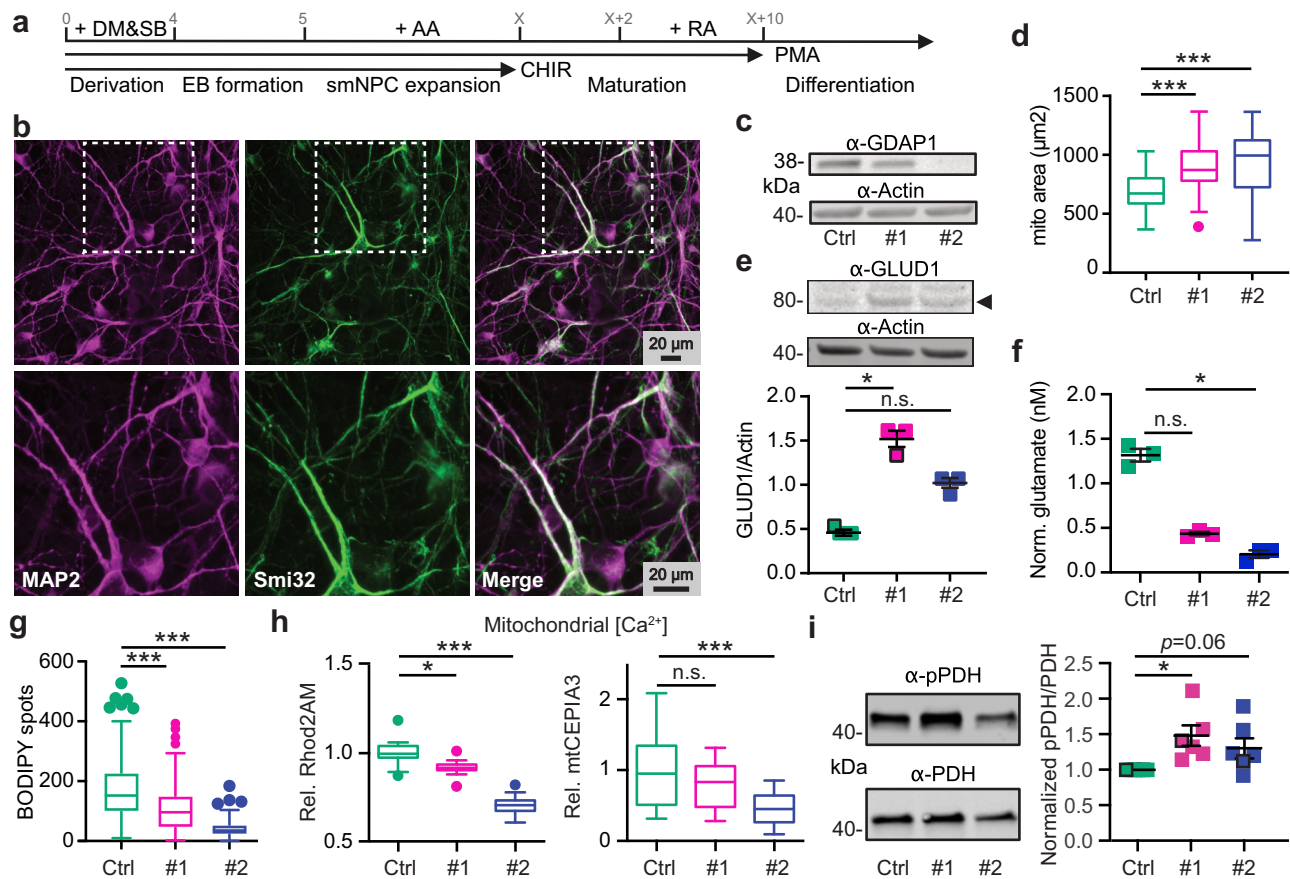


Fig. 4 Patient-derived cells are similarly characterized by an anaplerotic state and reduced mitochondrial Ca^{2+} levels. **a** Differentiation protocol to obtain motoneurons (MN) from induced-pluripotent stem cells (iPSCs) and **(b)** confirmatory immunocytochemistry by staining against dendrite marker MAP2 and motoneuronal neurofilament Smi32. **c** Immunoblot of total MN cell lysates for validation of GDAP1 expression, actin served as loading control, size is indicated. **d** Automated high-content microscopy analysis of MitoTracker-stained mitochondria revealed an increased total mitochondrial mass per well. **e** Immunoblot of total MN cell lysates demonstrated increased glutamate dehydrogenase (GLUD1, arrowhead) in patient-derived MNs, actin served as loading control. **f** Reduced glutamate levels in CMT4A patient-derived MN determined by a luminescence-based assay indicating increased glutamine consumption compared to Ctrl. **g** Automated high-content microscopy analysis of BODIPY-positive spots normalized to the nuclei area in MN revealed a reduced number of lipid droplets in CMT4A patient-derived cells. **h** Reduced relative mt $[\text{Ca}^{2+}]$ levels of NPCs determined by confocal microscopy with Rhod2-AM and mito-CEPIA3. **i** Immunoblots and quantification demonstrating increased phosphorylation of PDH E1 serine 293, normalized to total PDH E1 levels and control cells. Data in **(d–g)** were from 3 independent differentiations and data in **(d, g)** were obtained from $n > 40,000$ cells in quadruplicate, experiments in **(f)** were performed in duplicate. Data in **(h)** were from 20–22 Rhod2-AM-stained cells and 22–33 cells mitoCEPIA3 transfected from three independent experiments. Data in **(i)** were from 6 different passages. Data points corresponding to the example blots are highlighted. Statistical variation is shown as Tukey boxplots in **(d, e)** or scatter plots in **(i)** with mean \pm SEM indicated. Significance was calculated using the non-parametric Kruskal-Wallis test, * $p < 0.05$, ** $p < 0.001$, *** $p < 0.0001$.

potential as GDAP1 KD cells (Fig. 1) but also feature the same metabolic changes and alterations of Ca^{2+} levels. Together this suggests that GDAP1-mediated CMT4A is caused by inhibition of PDH activity resulting in an anaplerotic state.

GDAP1 knockdown reduces the number of contact sites between mitochondria and the endoplasmic reticulum. We suspected that changes in MERCS might underlie the changes in mitochondrial Ca^{2+} levels especially as a reduced colocalization of ER and mitochondrial markers hint to changes in MERCS, as shown previously¹⁹. MERCS are hot spots of interactions between the ER and mitochondria defined by a distance of mitochondrial and ER membranes between ~ 10 and ~ 50 nm³² and are important signaling hubs (reviewed in ref. 33). Using transmission electron microscopy, we indeed found (i) a decrease in MERCS in GDAP1 KD cells defined as the percentage of mitochondrial perimeter covered by the ER, (ii) a decreased number of MERCS

per mitochondrion, (iii) a decreased length of MERCS (Fig. 5a) and (iv) an increased width between the ER and mitochondria (Fig. 5a, b). As an additional readout to quantify the distance between mitochondria and the ER, we used a well-established assay based on Förster resonance emission transfer (FRET) between two fluorescent proteins targeted to the surface of mitochondria and the ER, both facing the cytosol^{34,35}. The lower FRET ratio (Fig. 5c) confirmed the data obtained by the morphometric analysis with an increased width between the organelles in GDAP1 KD cells. Comparing the amount of ER protein present in mitochondrial cell fractions using immunoblotting of the membrane ER protein Sec62 and the mitochondrial protein Cox4 also confirmed the reduction in contact sites (Fig. 5d). Such a reduction and increased distance should result in decreased Ca^{2+} transfer from the ER to the mitochondrial matrix. We studied this by triggering ER Ca^{2+} release with the cholinergic agent carbachol, which activates inositol trisphosphate receptors (IP3Rs) leading to Ca^{2+} release into the cytosol, generating Ca^{2+}

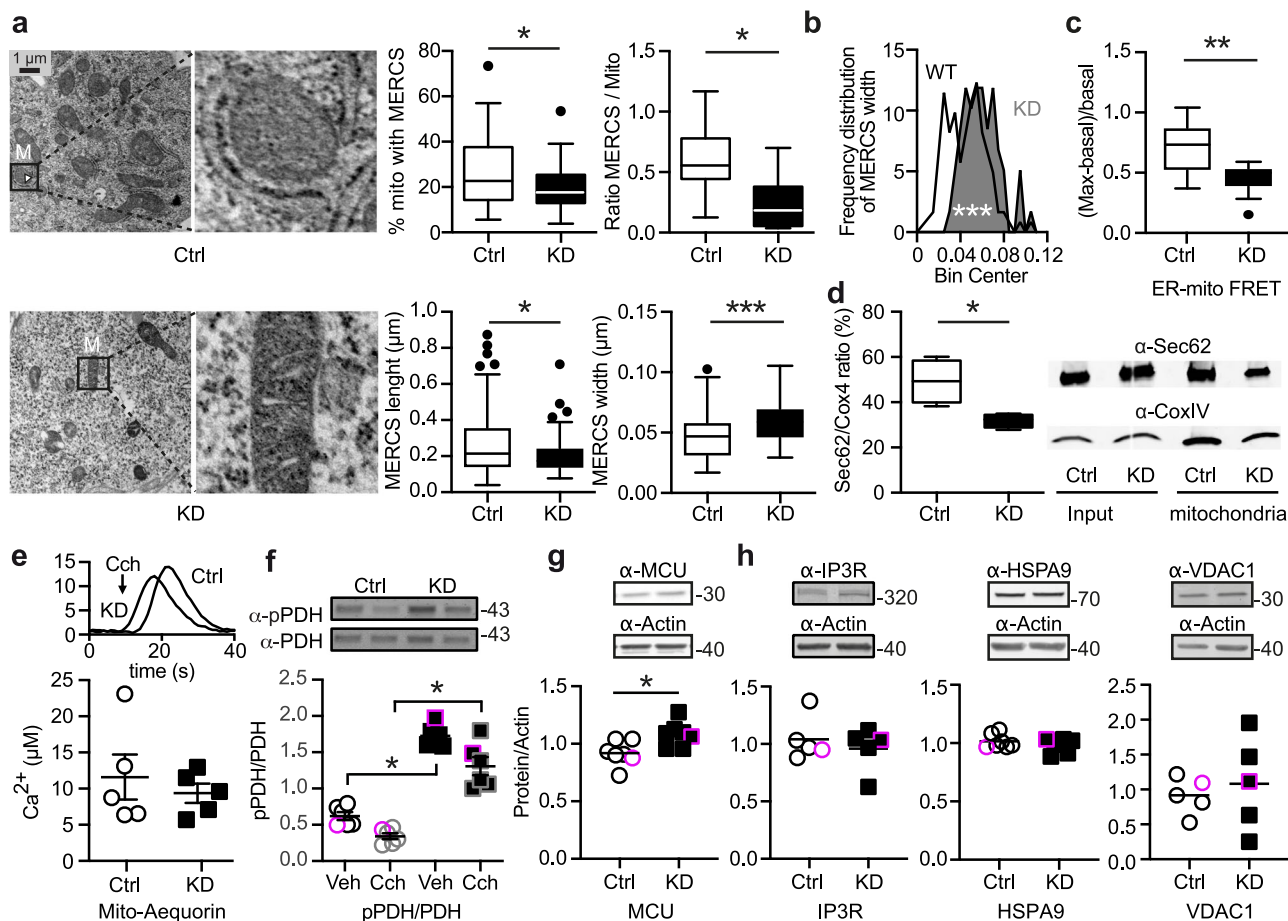


Fig. 5 GDAP1 knockdown reduces the number of contact sites between mitochondria and the endoplasmic reticulum. **a** Transmission electron microscopy of knockdown (KD) and control (Ctrl) cells. The indicated parameters were quantified using ImageJ by a blinded investigator. M, mitochondrion. **b** Histogram showing the distribution of MERCS' widths, and an increased distance in KD cells between the ER and mitochondria. **c** Proximity of ER and mitochondria was measured using a FRET-FEMP sensor comprising ER CFP-Sac1 and mitochondrial YFP-Akap1. Proximity leads to high intensity of YFP-FRET-emission (410–430/520–560 ex/em). 100 nM rapamycin was added to achieve the closest possible distance, and the measurement of FRET ratio was calculated as $(FRET_{max} - FRET_{basal}) / FRET_{basal}$. **d** Quantification of ER membrane (Sec62) and mitochondrial (Cox4) proteins in mitochondrial fractions. **e** Representative curve for the aequorin Ca²⁺ measurement and quantification of mitochondrial Ca²⁺ levels after addition of 200 μM carbachol (CCH), which releases Ca²⁺ from the ER by activation of a G-protein-coupled receptor. **f** Immunoblot of Ctrl and KD cells lysed 10 min after 200 μM CCH addition to quantify the PDH phosphorylation (pPDH/(PDH_{total})) after Ca²⁺ release into the MERCS and mitochondria. **g**, **h** Immunoblot of total cell lysates of Ctrl and KD cells showing increased expression levels of MCU but not pan-IP3R, HSPA9 or VDAC1, actin served as loading control, size is indicated. Data in **(a)** were obtained from 11 (Ctrl) and 9 (KD) cells, in **(b)** from 4 independent experiments in triplicate or quintuplicate with a range of 162–818 cells per experiment, and in **(d)** from 4 independent experiments. Data in **(e)** from 5 independent experiments performed in triplicates. Data points corresponding to the example blots are highlighted. Statistical variation is shown as Tukey boxplots or scatter plots with the indication of mean ± SEM and significance was calculated using the non-parametric Mann-Whitney test, * $p < 0.05$, ** $p < 0.001$, *** $p < 0.0001$.

microdomains at MERCS, which sustain rapid Ca²⁺ uptake by mitochondria^{34,36}. Surprisingly, we did not observe a difference in mitochondrial Ca²⁺ uptake measured by mitochondrially-targeted aequorin upon treatment with carbachol (Fig. 5e). The direct reducing effect of carbachol on PDH E1 phosphorylation was also similar in both cell lines while the baseline levels were significantly increased in GDAP1 KD cells (Fig. 5f). Apparently, upregulated MCU levels (Fig. 5g) and hyperpolarization (see Fig. 11) can compensate for the increased distance between the organelles under conditions of high Ca²⁺ influx. The other components of the ER-mitochondrial Ca²⁺ uptake complex³⁷, the IP3R ER Ca²⁺ release channels, the molecular chaperone glucose-regulated protein 75 (Grp75, official name Heat Shock Protein Family A (Hsp70) Member (HSPA)), and the mitochondrial voltage-dependent anion channel 1 (VDAC1) at the outer mitochondrial membrane were however similarly expressed in GDAP1 KD and control cells (Fig. 5h). Taken together our

findings support altered MERCS with an increased distance between the ER and mitochondria in GDAP1 KD cells.

Increased levels of proteins involved in β-oxidation in GDAP1 KD cells.

To clarify how GDAP1 KD affects MERCS and mitochondrial Ca²⁺ levels, we next set out to identify proteins that are dysregulated in KD cells by label-free quantitative liquid chromatography coupled to mass spectrometry (LC-MS)³⁸. Comparing the proteome of control and GDAP1 KD cells identified 985 significantly dysregulated proteins out of 3914 proteins—456 proteins were found to be less abundant and 529 to be more abundant (Fig. 6a). Then, we submitted the list of upregulated proteins to STRING³⁹ and observed that the following KEGG (Kyoto Encyclopedia of Genes and Genomes) pathways were over-represented with a false-detection rate below 2×10^{-4} : protein processing in the ER, lysosome, regulation of the actin cytoskeleton, endocytosis, fatty acid degradation and citrate cycle

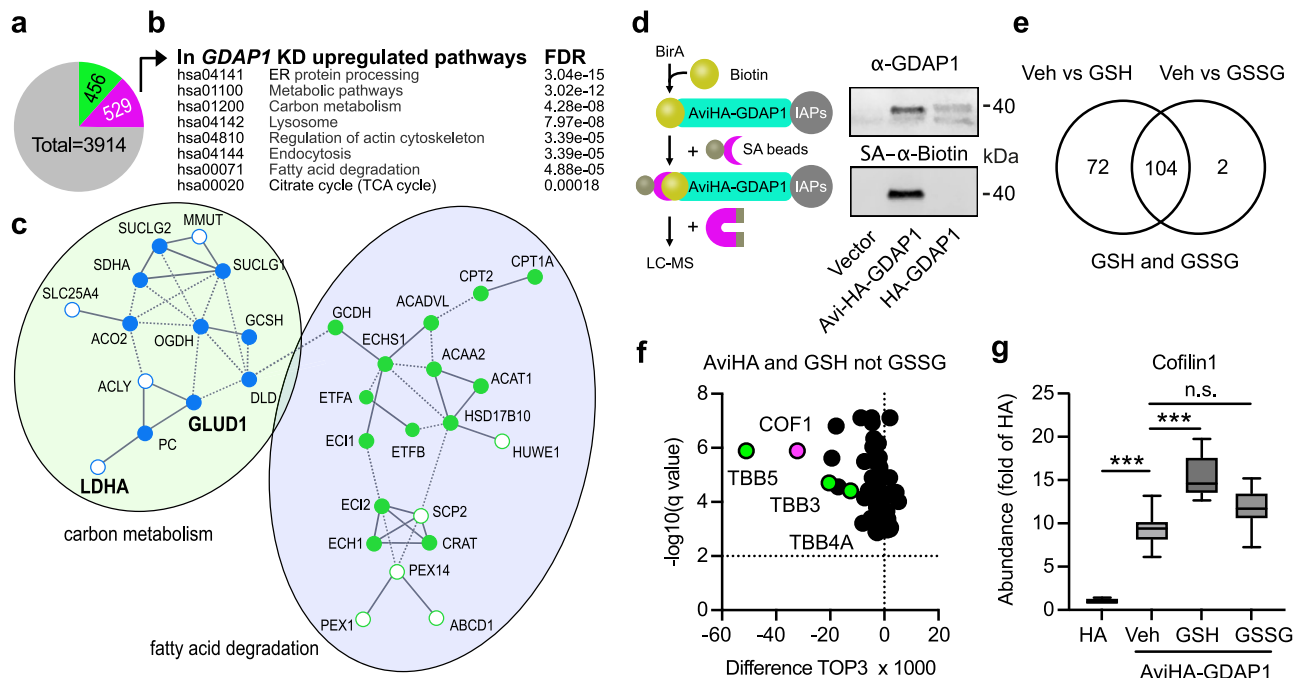


Fig. 6 LC-MS proteomics identifies proteins involved in β -oxidation as being more abundant in *GDAP1* KD cells and hints to alterations of the actin cytoskeleton mediated by redox-dependent interactions with *GDAP1*. **a** Number of proteins dysregulated in *GDAP1* KD cells identified by label-free proteomics from three independent experiments, measured in quadruplicates, green less abundant, magenta more abundant. Statistical significance was determined by Student's *t* test with Bonferroni correction. **b** KEGG pathways significantly altered in proteins more abundant in *GDAP1* KD cells. **c** Section of a STRING analysis of proteins more abundant in *GDAP1* KD cells corroborating altered carbon metabolism (blue) and fatty acid degradation (green) in these cells. Open dots correspond to more abundant interacting proteins that do not fall directly into these categories. Proteins in bold were found to be more abundant independently using immunoblotting. **d** Schematic illustration showing the biotinylation of the AviTag fused to *GDAP1* protein and subsequent pulldown and enrichment of biotinylated *GDAP1* protein via streptavidin-labeled magnetic beads. Immunoblot of cell lysates prior to pulldown of biotinylated *GDAP1* stained against *GDAP1* and Biotin with an infrared-labeled streptavidin (SA) dye shows an overlap of biotinylation and *GDAP1* protein. Streptavidin pulldown was performed with primary neuronal cultures from BirA-expressing E16 mouse embryos. **e** Results from label-free quantitative proteomics performed with GSH or GSSG added to the preparation, **(f)** shows the 72 proteins with an altered expression after addition of GSH but not GSSG. **g** TOP3 quantification of Cofilin-1 abundance and increased Cofilin-1 abundance upon GSH, but not GSSG addition indicated an interaction with *GDAP1* in a redox-dependent manner. Statistical significance in **g** was determined by one-way ANOVA and the Tukey test, *** $p < 0.0001$.

(Fig. 6b). The analysis corroborated the increased levels of LDHA and *GLUD1* observed by immunoblotting (Fig. 2c). It also demonstrated increased levels of proteins involved in β -oxidation (Fig. 6c) like carnitine palmitoyltransferase 1 (*CPT1A*) which catalyzes the transfer of the acyl group of long-chain fatty acid-CoA conjugates onto carnitine to transport the resulting acyl-carnitine long-chain fatty acids inside the mitochondria. These results suggest that the decrease in lipid droplets observed in *GDAP1* KD cells (Fig. 2f) indeed reflects a high lipid catabolism that serves to provide the TCA cycle with acetyl-CoA.

GDAP1 interacts with proteins of the actin cytoskeleton in a redox-dependent manner. We then used label-free proteomics to identify *GDAP1*-interacting proteins to get a more complete picture of how *GDAP1* loss of function affects cellular metabolism. We transduced primary cortical cultures from mice expressing the biotin ligase BirA⁴⁰ with adeno-associated viruses expressing *GDAP1* tagged with an Avi-tag, a specific substrate for BirA⁴¹. Only Avi-HA-tagged *GDAP1* but not the HA-tagged control was biotinylated (Fig. 6d). By treating the mitochondrial preparations with GSH or GSSG as described⁴², we further aimed to identify proteins whose interaction is affected by their specific redox state. This was driven by the fact that *GDAP1* can bind potential GST substrates^{9,10} and the assumption that such an interaction might depend on the local redox environment. A total of 268 proteins were pulled down from Avi-HA but not or less from HA-*GDAP1*-transduced cultures. 176 of these proteins

showed a statistically different abundance in preparations treated with GSH compared to vehicle and 106 in preparations treated with GSSG. For 72 proteins the interaction with *GDAP1* was altered only by GSH and not by GSSG treatment (Fig. 6e). Interestingly, the most strongly and most significantly regulated proteins can be linked to the cytoskeleton like tubulins (Fig. 6f, green), crucial components of the cytoskeleton that can serve as a scaffold for mitochondrial transport⁴³. This is consistent with regulation of the actin cytoskeleton being one of the top hits in the KEGG analysis of proteins upregulated in *GDAP1* KD cells (Fig. 6b, Supplementary fig. 3). In addition, an interaction between *GDAP1* and β -tubulin *TUBB* has been reported in a yeast-two-hybrid experiment⁴⁴. This led us to further concentrate our subsequent analysis on a potential misregulation in actin dynamics in CMT4A-disease models.

GDAP1 knockdown reduces Cofilin-1 abundance at mitochondria. The actin-regulatory protein Cofilin-1 (Fig. 6g) specifically caught our attention because it affects mitochondrial shape by inducing depolymerization of actin filaments in mitochondrial proximity which restricts access of *DRP1* to mitochondria²¹. Its antagonist is the ER-anchored *INF2*, which also causes CMT disease when mutated²⁰. We further explored the identified interaction between *GDAP1* and Cofilin-1, and hypothesized that *GDAP1* alters actin abundance, polymerization or both at mitochondrial sites by interacting with Cofilin-1. The actin-binding ability of Cofilin-1 is inhibited by phosphorylation of serine 3

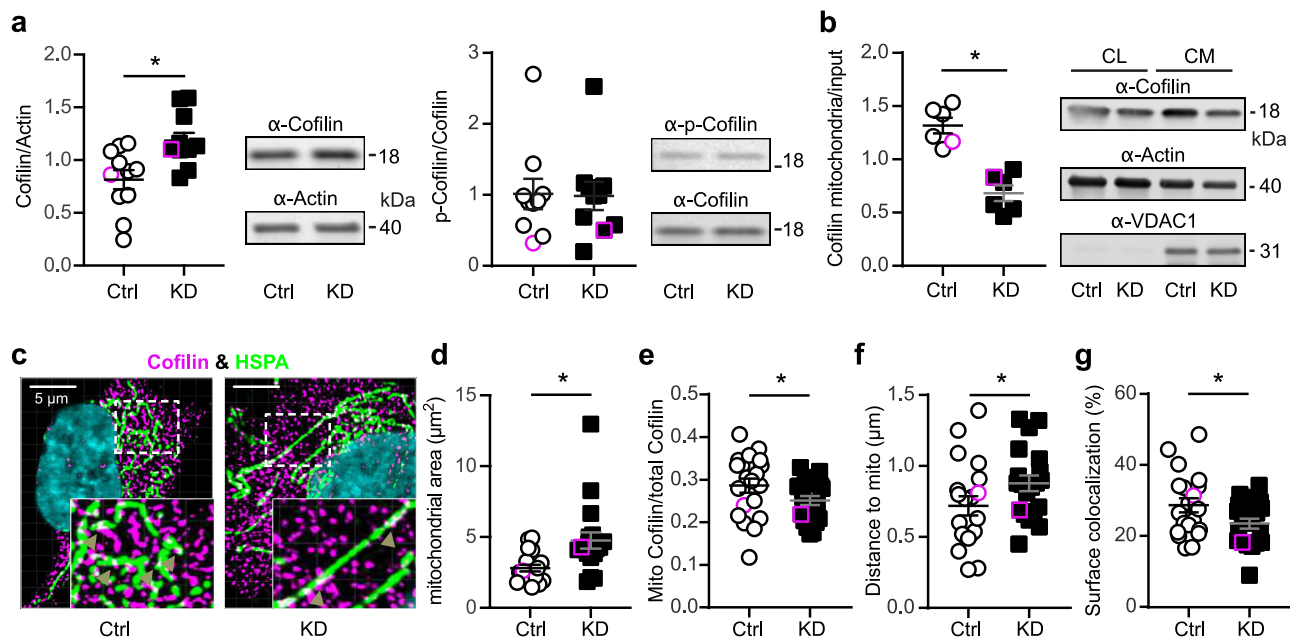


Fig. 7 Reduced presence of Cofilin-1 at mitochondria. **a** Immunoblot of whole cell lysates and quantification of Cofilin-1 and p-Cofilin-1 (S3) protein levels. Actin served as loading control. **b** Analysis of Cofilin-1 abundance at the mitochondria after fractionation of crude mitochondria (CM) normalized to Cofilin-1 levels in whole cell lysates (CL). **c** Immunostaining of Ctrl and *GDAP1* KD cells for Cofilin-1 and HSPA9 as mitochondrial protein. Nuclei were counterstained with DAPI. Imaris analysis confirmed **(d)** the increased mitochondrial area in KD cells and **(e)** a reduction of mitochondrially-located Cofilin-1 (white, arrowheads) concomitant with **(f)** an increased distance between mitochondria and cofilin-1. Conversion of the structures into surfaces using contact XTension demonstrated **(g)** that the proportion of the mitochondrial surface area in contact with Cofilin-1 was significantly reduced. **d, f** Data are from a total of $n = 20$ cells per cell line from three independent experiments. Data points corresponding to the example are highlighted. Statistical variation is shown as scatter plots with the indication of mean \pm SEM and significance calculated using the non-parametric Mann-Whitney test, $*p < 0.05$.

which is controlled by the presence of intramolecular disulfide bridges^{45,46} or protein glutathionylation⁴⁷ and could thus be a target of *GDAP1*'s GST activity. Alternatively, *GDAP1* could just recruit Cofilin-1 to the mitochondrial surface in a redox-dependent manner. We studied Cofilin-1 abundance and intracellular localization and phosphorylation in *GDAP1* KD and control cells. *GDAP1* KD increased the total abundance of Cofilin-1 but did not affect phosphorylation (Fig. 7a). However, when we compared the protein levels in mitochondrial fractions, we observed the opposite, a significant reduction in *GDAP1* KD cells (Fig. 7b). To further test for the amount and localization of Cofilin-1 close to mitochondria, we used HSPA9, a mitochondrial matrix protein, as a marker as it was not regulated in *GDAP1* KD cells (Fig. 5h) and plays a role in ER-mitochondrial Ca^{2+} transfer³⁷. Confocal microscopy demonstrated an increase in the area covered by mitochondria (Fig. 7c and d) in line with the more tubular network in *GDAP1* KD cells (Fig. 1h) and a reduction of mitochondrial Cofilin-1 compared to total Cofilin-1 in *GDAP1* KD cells (Fig. 7e), in line with the fractionation assays. In addition, the distance of Cofilin-1 spots from mitochondria was significantly increased (Fig. 7f) and the colocalization of the surfaces of Cofilin-1 and HSPA9-expressing structures was reduced (Fig. 7g). These results imply that *GDAP1* controls the presence of Cofilin-1 in proximity to the mitochondrial surface, possibly at MERCS.

***GDAP1* KD reduces F-actin fibers at mitochondrial surfaces and restricts access of DRP1 to the mitochondria resulting in less DRP1 and MFF.** Because Cofilin-1 is an actin-binding protein, we suspected less actin in the proximity of mitochondria in *GDAP1* KD cells. We quantitated F-actin levels and its colocalization with mitochondria in living cells by transiently transfecting control and *GDAP1* KD cells with GFP-tagged F-tractin and

labeling of mitochondria with mitotracker red. F-tractin does not perturb actin rearrangement^{48–50} and was previously used to study the effects of INF2 perturbation on mitochondrial dynamics^{18,51}. Our data revealed a significant reduction of surface colocalization between F-actin and mitochondria in *GDAP1* KD cells (Fig. 8a) in line with our hypothesis. As expected from previous work¹⁷, this severely reduced DRP1 localization in mitochondrial fractions (Fig. 8b). The decreased colocalization of DRP1 with mitochondria was also evident when we overexpressed GFP-tagged DRP1 in control and *GDAP1* KD cells (Fig. 8c). Interestingly, DRP1 also covered less space in *GDAP1* KD cells (Fig. 8d). To rule out that this is caused by a reduced transfection efficiency, we quantified total endogenous DRP1. This also revealed a reduced abundance of DRP1 and its receptor at the mitochondrial surface, mitochondrial fission factor (MFF) (Fig. 8e). In summary, these findings imply that in the absence of *GDAP1*, F-actin fibers are less present at the mitochondrial surface which restricts the access of ER tubules and DRP1 to sites of mitochondrial constriction and decreased levels of DRP1 and its receptor MFF resulting in a dysfunction of mitochondrial dynamics (Fig. 8f).

Discussion

In this work, we used neuronal *GDAP1* KD in human SH-SY5Y neuroblastoma cells and patient-derived cells to study the pathophysiology of CMT4A. We found that *GDAP1* interacts with the actin-interacting protein Cofilin-1 and that loss of *GDAP1* results in a reduction of F-actin fibers in mitochondrial proximity. This limits the access of ER tubules to mitochondria which connects two processes: it impedes DRP1 recruitment to mitochondrial constriction sites resulting in more tubular mitochondria and it disrupts mitochondria-ER contact sites causing reduced mitochondrial Ca^{2+} levels. The reduced mitochondrial

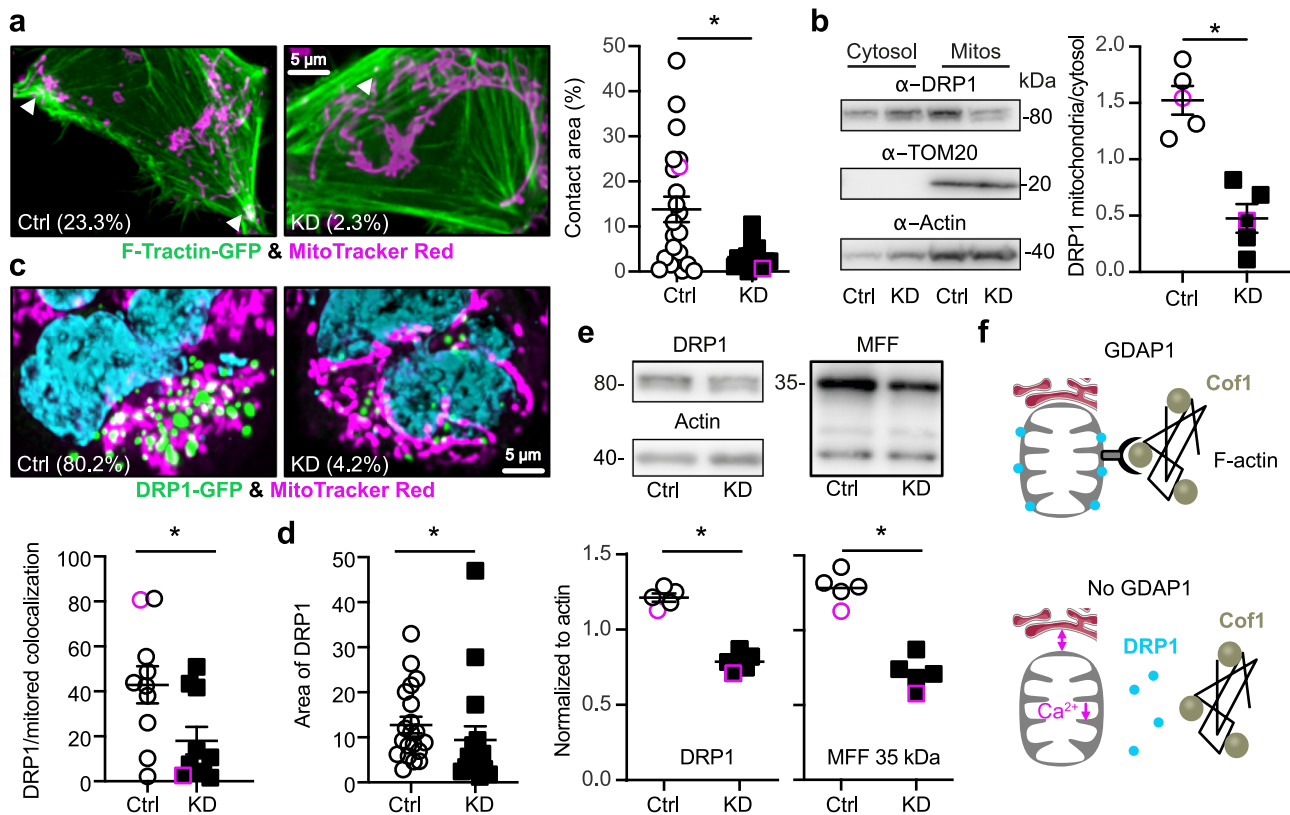


Fig. 8 GDAP1 KD reduces F-actin fibers at mitochondrial surfaces and restricts access of DRP1 to the mitochondria resulting in less DRP1 and MFF.

a Live cell imaging of GFP-F-tractin transfected cells. Mitochondria were stained with MitoTracker and images analyzed for contact area using Imaris. **b** Immunoblot of DRP1 in cytosolic and mitochondrial fractions demonstrating a reduced DRP1 abundance in mitochondrial fractions. TOM20 and actin served as loading controls, size is indicated. **c, d** Live cell imaging of GFP-DRP1 transfected cells. Mitochondria were stained with MitoTracker and images analyzed for **(c)** colocalization and **(d)** area. **e** Immunoblot of total DRP1 and MFF demonstrating a reduced abundance of both proteins. Actin served as loading control, size is indicated. **f** Scheme depicting our findings. Cof1, Cofilin-1. In the absence of GDAP1 mitochondrial F-actin is reduced resulting in an increased distance between ER and mitochondria, reduced mitochondrial Ca^{2+} levels, and a reduced presence of DRP1 at mitochondrial constriction sites. Data from **(a)** are from $n = 19$ cells per cell line from three independent experiments performed in triplicates. Data from **(c)** are from $n = 10$ and **(d)** from $n = 16$ cells per cell line from three independent experiments. Data points corresponding to the examples are highlighted. Statistical variation is shown as scatter plots with the indication of mean \pm SEM and significance calculated using the non-parametric Mann-Whitney test, $*p < 0.05$.

Ca^{2+} levels inhibit the PDC and result in a rewired cellular metabolism characterized by dependence on glutamine and fatty acids to compensate for an impaired TCA cycle. We therefore conclude that the reduction in F-actin presence at mitochondria caused by GDAP1 loss of function represents the probable cause of autosomal-recessive CMT4A.

The reduced mitochondrial Ca^{2+} levels in GDAP1 KD and GDAP1-loss-of-function NPCs are difficult to understand because over-expression of the MCU was shown previously to increase the matrix Ca^{2+} concentration⁵². Other, unchanged components of the ER-mitochondrial complex that regulate Ca^{2+} transfer, such as the ER release channels, the mitochondrial VDAC1 channels and the linking protein HSPA9 (Grp75)³⁷ (Fig. 5h) might account for this. In addition, the amount and stoichiometry of the MCU-interacting proteins MICU1 and MICU2, which are regulatory subunits of the large protein complex which mediates mitochondrial Ca^{2+} uptake, also affect the matrix Ca^{2+} concentration⁵² and were not further studied here as it is difficult to fathom how the outer mitochondrial membrane protein GDAP1 could affect or modify these proteins. Despite the reduction in MERCs in GDAP1 KD cells, agonist-induced increases in mitochondrial Ca^{2+} levels were unchanged. Such Ca^{2+} transients are believed to instigate the increase in PDC activity^{28,29}. We therefore have to conclude that the reported blunting of the Ca^{2+} -dependent increase of mitochondrial

respiration upon SOCE²² also affects PDC activity. In line with this, it was recently shown that in mouse *Gdap1*^{-/-} motoneurons, glutamate treatment results in a decreased decay of the Ca^{2+} signal and a reduction in respiration⁵³. The authors attributed this to defects in mitochondrial movement resulting in a lack of correct positioning of mitochondria at sites where an intense stimulation of ATP production by oxidative phosphorylation is required like the plasma membrane. Interestingly, the actin cytoskeleton is essential for short-distance mitochondrial movements and for immobilization of mitochondria at the actin cortex, a specialized layer of cytoplasmic proteins on the inner face of the cell membrane (reviewed in⁵⁴) suggesting that the changes described here could also underlie these defects in mitochondrial positioning. Alternatively, other yet unknown mechanisms exist that link the actin cytoskeleton to steady-state mitochondrial Ca^{2+} levels.

We found that GDAP1 interacts with Cofilin-1 in a redox-dependent manner and restricts its presence at the mitochondrial surface. This was shown by confocal microscopy using HSPA9 as a marker protein. HSPA9 (Grp75) is recognized to be enriched in MERCs. An enrichment of Cofilin-1 in MERCs has not been reported yet and we reproduced the reduced abundance of Cofilin-1 in *GDAP1* KD cells in fractions containing crude mitochondria (Fig. 7b). We therefore conclude that the reduction of Cofilin-1 at mitochondrial surfaces is not restricted to MERCs.

Very recently, Cofilin-1 was shown to affect mitochondrial shape and function⁵⁵. Theoretically, GDAP1 could affect Cofilin-1 function through its still unresolved potential GST-like enzymatic activity^{6,8–10} because Cofilin-1 contains four potential GST target cysteine residues at the positions 39, 80, 139 and 147. Cysteines 39 and 80 are buried inside the protein while cysteines 139 and 147 are located on the surface of the protein⁵⁶. Redox-mediated modifications of these cysteine residues clearly affect the function of Cofilin-1. Treatment with hydrogen peroxide leads to the formation of an intramolecular disulfide bond resulting in a conformational change that prevents phosphorylation and thereby actin polymerization⁴⁵. Moreover, intermolecular disulfides and oligomeric forms of Cofilin-1 have been described. Monomeric Cofilin-1 possesses severing activity, whereas the dimeric and oligomeric forms have actin-bundling activity⁵⁷. Interestingly, only monomeric Cofilin-1 is phosphorylated⁵⁸ which represents the most-studied post-translational modification of Cofilin-1 to date. Cofilin-1 can be post-translationally modified by phosphorylation of serine 3. Increased phosphorylation inhibits the actin-binding ability of Cofilin-1⁵⁹; dephosphorylated Cofilin-1 preferentially localizes to mitochondria, whereas a mutation mimicking the phosphorylated protein prevents translocation from the cytosol to mitochondria⁶⁰. We found no changes in Cofilin-1 phosphorylation in whole cell lysates and no phosphorylated Cofilin-1 in mitochondrial fractions. Upon oxidation of all four cysteine residues and dephosphorylation at serine 3, Cofilin-1 loses its affinity for actin, translocates from the cytosol to mitochondria and induces apoptosis^{60,61}. Oxidation of methionine 115 apparently also prevents its actin depolymerization activity and induces forced mitochondrial translocation and apoptosis⁶². In addition, Cofilin-1 can be glutathionylated, which represents the presumed enzymatic activity of GDAP1. Glutathionylation of Cofilin-1 was demonstrated in lymphocytes treated with the thiol-oxidizing reagent diamide⁶³ and in cells of the rat nucleus accumbens during cued cocaine seeking in the absence of cocaine⁴⁷. Interestingly, glutathionylation reduces cofilin-1-dependent depolymerization of F-actin, implying regulatory functions in cell signaling⁴⁷. It remains to be clarified whether GDAP1 affects the redox state and function of Cofilin-1 by specific glutathionylation.

Mutations in other proteins that target the same pathway also cause CMT disease. Mutated PDK3 also inhibits the PDC by hyperphosphorylation of the PDH E1 α subunit similar to GDAP1 loss of function. This causes CMTX6²⁴. Loss of function of the actin-polymerizing protein INF2 alters mitochondrial shape by changing DRP1 access to mitochondria similar to GDAP1 KD¹⁷. INF2 is also implicated in the abundance of MERCS and changes in mitochondrial Ca²⁺ dynamics¹⁸ which we also observed in GDAP1 loss-of-function cells. Mutations in INF2 also cause CMT disease, CMTDIE²⁰. Mutations in Dynamin-2 (DNM2), a ubiquitously expressed large GTPase that interacts tightly with the actin and microtubule network^{64,65} also cause CMT disease, dominant intermediate CMT (CMTDIB)⁶⁶ and autosomal-dominant CMT2M⁶⁷. Similar to GDAP1, DNM2 works in concert with DRP1 to orchestrate mitochondrial constriction events that result in division⁶⁸. DNM2 therefore directly interferes with the same processes that we found to be affected by GDAP1 loss of function. Finally mutations in BSCL2 (Bernardinelli-Seip Congenital Lipodystrophy Type 2) also known as seipin cause a distal hereditary motor neuropathy (HMN5C) which can present with features of axonal CMT2⁶⁹. BSCL2 is an ER protein crucial in the formation of lipid droplets^{70,71}. BSCL2 also interacts with the adaptor protein YWHAB (14-3-3- β) which then recruits cofilin-1 to remodel the actin cytoskeleton for adipocyte differentiation⁷².

In summary, our results shed light on the pathophysiology of CMT4A and highlight the importance of GDAP1 and actin for

mitochondrial function. The fact that mutations in diverse proteins that all interact with the overarching mechanisms described here—metabolic and mitochondrial remodeling caused by changes in the interaction of the actin cytoskeleton with mitochondria—cause CMT disease strengthens the importance of this mechanism for the health of the peripheral nervous system.

Methods

Generation of iPSCs. iPSC lines from two CMT4A patients and one healthy donor were generated with Sendai virus (CytoTune, DNASVEC Corporation) coding for POU5F1, SOX2, KLF4 and MYC. All subjects gave written informed consent prior and the study was approved by the local ethics committee at the Universities of Warsaw (patient #1), Düsseldorf (patient #2) and Bonn (healthy donor). In brief, Sendai virus-infected primary fibroblasts were immediately centrifuged for 45 min at 32 °C with 1500 g (spinfection) and cultivated in Advanced DMEM containing 5% fetal calf serum (FCS) and 1% GlutaMAX™ (all from Life Technologies). On the following day the virus-containing medium was replaced with fresh culture medium. Five days post infection (d5), transduced fibroblasts were trypsinized and seeded onto mouse feeder-coated dishes in DMEM/F-12 containing 10% Knock-Out™ Serum Replacement, 1% nonessential amino acids (NEAA), 1% GlutaMAX™, 1% pyruvate, 0.1 mM β -mercaptoethanol and 10 ng/ml basic fibroblast growth factor (bFGF) (all from Life Technologies). Medium was changed every other day until clonal iPSC colonies were manually picked and adapted to feeder-free culture conditions. Several clonal lines were subjected to SNP genotyping in order to identify iPSC clones with normal karyotype.

SNP analysis of iPSC lines. Genomic DNA was prepared using the DNeasy Blood & Tissue Kit (Qiagen). Whole-genome single nucleotide polymorphism (SNP) genotyping was performed at the Institute of Human Genetics at the University of Bonn. Genomic DNA at a concentration of 60 ng/ μ L was used for whole-genome amplification. Afterwards, the amplified DNA was fragmented and hybridized to sequence-specific oligomers bound to beads on an Illumina HumanOmniExpress-12v1.0 chip. Data were analyzed using Illumina Bead Studio.

Differentiation of hiPSCs into neural cells. Induced-pluripotent stem cells were grown using mTESR™1 medium (Stemcell Tech., 05850) on matrigel (Corning, 354277). Human iPSC cells were detached from matrigel using ReLeSR™ (Stemcell Tech., 05872), resuspended in medium consisting of Dulbecco's modified Eagle's medium/ F12 supplemented with 10% knockout serum (Invitrogen, 10828-028), 1% N2 supplement (Gibco, 17502-048), 0.05% B27 (Gibco, 17504-044), 20 ng/ml epidermal growth factor (Sigma, E9644) and 10 ng/ml basic fibroblast growth factor (Gibco, PHG0024), and plated within a low-attachment petri dish to induce embryoid body (EB) formation for 4 days. The EBs were plated on polyornithine (Sigma, P3655)/laminin (Sigma, L2020)-coated dishes for additional 6 days to induce the formation of neural rosettes. Neural rosettes were then manually removed, dissociated with accutase (Stemcell Tech., 07920), plated on poly-L-ornithine/laminin-coated dishes, and then treated with 3 μ M retinoic acid for 7 days. The medium was changed daily and cultures were passaged weekly by accutase and plated on matrigel-coated dishes in the above-mentioned neural medium.

Small molecule differentiation of hiPSCs into motoneurons. iPSCs differentiation was performed by the addition of small molecules adapted from a previously described protocol⁷³. Briefly, for neuronal induction, iPSCs were seeded as colonies resuspended in E8 medium 2 days prior differentiation. To start the differentiation, medium was changed to N2B27 medium (50% Neurobasal medium/ 50% DMEM-F12 medium with 1:200 N2 supplement, 1:100 B27 supplement without vitamin A and 1% penicillin, streptomycin and L-glutamine respectively) supplemented with the small molecules 10 μ M SB-431542 (SB), 1 μ M dorsomorphin (DM), 3 μ M CHIR 99021 and 0.5 μ M PMA for four days. Subsequently, SB and DM were replaced by 150 μ M Ascorbic Acid (AA), and cells were fed daily until epithelium-like structures emerged. Neural epithelial structures were picked, dissociated mechanically and plated on 12-well plates, which were coated with Matrigel (1:100 in DMEM/F12) overnight. After around five passages the smNPC cells reached a high purity and were further kept in culture on Matrigel-coated plates and N2B27 medium supplemented with CHIR, PMS and AA. Detaching of the cells for passaging was performed with accutase. Starting from smNPC passage 13, differentiation to MN could be initiated. N2B27 medium with 1 μ M PMA was added 3 days after passaging. After two more days, 1 μ M retinoic acid (RA) and 1 μ M PMA were supplemented to the medium for the following 8 days, until culturing in maturation medium began, consisting of N2B27 medium with BDNF, GDNF and dbcAMP for two more weeks.

Immunoblotting. Denatured total cellular protein samples were separated on SDS polyacrylamide gels 4–15% Mini-PROTEAN® TGX Stain-Free™ gels (Bio-Rad) and transferred onto a nitrocellulose membrane using the Trans-Blot® Turbo™ Transfer System (Bio-Rad). Membranes were blocked with 3% (w/v) milk powder in PBS-T

or TBS-T (1x PBS or TBS, 0.05% (v/v) Tween 20) for 1 h at room temperature (RT). Chameleon Duo Pre-stained Protein Ladder (Li-Cor Biosciences) was used as a molecular weight standard. Primary antibodies were anti-actin mAb (clone C4, 1:4000; Millipore MAB1501), anti-Cofilin-1 mAb (clone D3F9, 1:1000, Cell Signaling, 5175), anti-p-Cofilin-1 mAb (Ser3, clone 77G2, 1:1000, Cell Signaling 3313), anti-DRP1 mAb (clone 4E11B11, 1:1000, Cell Signaling 14647), anti-GDAP1 (1:750, Sigma HPA014266), anti-G6PD mAb (clone D5D2, 1:1000, Cell Signaling 12263), anti-GAPDH mAb (clone 14C10, 1:2000, Cell Signaling 2118), anti-GLUD1 mAb (clone D9F7P, 1:1000, Cell Signaling 12793), anti-HK1 mAb (clone C35C4, 1:1000; Cell Signaling 2024), anti-HK2 mAb (clone C64G5, 1:1000, Cell Signaling 2687), anti-HSPA9 (clone N52A/42, 1:1000, UC Davis/NIH NeuroMab Facility, Davis, USA, 73-127), anti-LDHA mAb (clone C4B5, 1:1000, Cell Signaling 3582), anti-MCU (1:1000, Sigma HPA016480), anti-MFF (1:1000, Proteintech 17090-1-AP), anti-MFN2 mAb (clone M03, 1:500; Abnova H00009927-M03), anti-Nestin mAb (clone rat-401, 1:1000, Merck chemicals MAB353), anti-PDH mAb (E1a, clone C54G1, 1:1000, Cell Signaling 3205), anti-PDH mAb (E2,E3bp, clone 13G2AE2BH5, 1:1000, Abcam, ab110333) anti-p-PDH (Ser293, 1:1000, Cell Signaling 31866), anti-PKM1/2 mAb (clone C103A3, 1:1000, Cell Signaling 3582), anti-TOM20 (1:1000, Sigma HPA011562), anti- β -III-Tubulin mAb (clone TuJ-1, 1:1000, R&D Systems MAB1195), anti-VDAC1 (clone 20B12AF2, 1:1000, Abcam ab14734). The membranes were incubated with the primary antibodies overnight at 4 °C. For visualization, membranes were incubated with an infrared fluorescence IRDye® 680RD Streptavidin for biotinylation staining or IRDye 800-conjugated anti-mouse, 800-conjugated anti-rabbit, or 680-conjugated anti-mouse IgG secondary antibody (1:15,000; Licor), for 1 h at RT and detected with the Odyssey Infrared Imaging System (Licor). Western Blots were analyzed with the Image Studio Lite Software (Li-Cor Biosciences).

Immunocytochemistry. Neuronal cells were grown on matrigel-coated μ -Slide 8 Well, ibiTreat (Ibidi, 80826), fixed with 4% paraformaldehyde (PFA) (CarlROTH, 3105.2) and permeabilized by 0.25% (v/v) Triton X-100 in PBS. Unspecific binding of antibodies was blocked with 1X Roti®-Block (CarlROTH, A151.4) for 30 min. Primary antibodies anti-Nestin (1:100, Ebioscience, 14-9843-82), anti-MAP2 (1:500, Synaptic Systems, 188004), anti-Smi32 (Clone SMI32, 1:1000, Biologend 801702), anti- β -III tubulin (1:1000, R&D Systems, MAB1195) were treated in 1X Roti®-Block at 4 °C overnight. The cells were washed three times with PBS and incubated with the fluorescent conjugated secondary antibody (Molecular Probes, A-11001) in 1X Roti®-Block for 1 h at RT. Subsequently, three PBS washing steps were done. Nuclei were stained with 300 nM 4',6-diamidino-2-phenylindole (DAPI). Pictures were taken with a Leica TCS SP5 inverted confocal microscope with a 63x/NA1.4 oil immersion objective, a BX51 Fluorescence microscope (Olympus) with a 20x objective or an Opera Phenix™ spinning disc high-content screening microscope (Perkin Elmer, USA) equipped with two 16-bit sCMOS cameras and a 40x, 1.1 NA water immersion objective. For Cofilin-1 evaluations, SH-SY5Y cells were grown on 12 mm glass cover slides. Primary antibodies were anti-Cofilin-1 mAb (clone D3F9, 1:100, Cell Signaling, 5175), anti-GRP75 mAb (clone N52A/42, 1:20, Neuromab 75-127). Pictures were taken with a Leica TCS SP8 inverted confocal microscope with a 63x/1.4 NA oil immersion objective in z-stacks. Images were analyzed in Imaris 9.5.1 (Bitplane). For motoneurons analysis, images were imported into marcopolo columbus database and underwent batch analysis that determined the fluorescence intensity of each marker. The signal intensities of Smi32 and MAP2 were normalized to β -tubulinIII each.

Confocal microscopy and image analysis. High-content light microscopy analysis was conducted with the Opera Phenix™ spinning disc microscope. Fluorescence (Ex/Em) with Hoechst, MitoTracker™ Green FM and tetramethylrhodamine methyl ester perchlorate (TMRM) was measured at 405/435-480, 488/500-550 and 561/570-630 nm ex/em, respectively. BODIPY™ 558/568 C12 was added to the cells in parallel to MitoTracker in a final concentration of 1 μ M for 15 min and subsequently, cells were incubated with normal growth medium. The images were analyzed with the software packages Harmony (version 4.5) and Columbus (version 2.7.1) containing the PhenoLOGICTM machine learning plugin (Perkin Elmer). Cells were selected via nuclear staining with HOECHST, but the cytosol region was defined using the mitochondrial stain. Within this selection, mitochondria and LDs were defined as isolated populations and analyzed respectively for their area and intensity. For mitochondria-associated LDs, the intensity of BODIPY™ 558/568 C12 staining was determined within the mitochondrial area. The complete image analysis sequences are available upon request. Live-cell imaging of actin filament analysis was conducted two days after transfection of GFP-F-tractin (gift of Henry N. Higgs, Dartmouth University) and together with staining of mitochondria with 100 nM MitoTracker™ Red CMXRos. Cells were imaged using the Leica TCS SP8 inverted confocal microscope with a 63x/1.4 NA oil immersion objective in z-stacks. Cells were captured at 1024x1024 with sequential image capturing. Step size was set at 0.25 μ m. Images from confocal microscopy for Cofilin-1, HSPA9 and actin filament quantification were analyzed in Imaris 9.5.1 (Bitplane). To improve the signal-to-noise ratio, iterative deconvolution was performed (Huygens Essential 20.10). The software then created 3D surfaces of mitochondria and Cofilin-1 spots to measure the surface area and to determine the shortest distance from the Cofilin-1 surface to the mitochondrial surface. Colocalizing Cofilin-1/actin with a distance \leq 0 μ m was duplicated to a

new surface and taken for the Imaris surface-surface contact XTension to quantify the contact area, defined as the percentage of mitochondrial surface contacting Cofilin-1. Similarly, 3D surfaces of Actin and the mitochondria were created. The software computed the contact area between the two surfaces as well as the shortest distance between the actin and mitochondria surfaces. Live-cell imaging of DRP1 surface analysis was conducted two days after transfection of pcDNA3-GFP-DRP1 (gift of Prof. Dr. Culmsee, Philipps-Universität Marburg) and together with staining of mitochondria with 100 nM MitoTracker™ RedCMXRos. Images were captured in a similar manner using the Leica TCS SP8 inverted confocal microscope. Images were then imported to and analyzed in Imaris 9.7.2 (Bitplane) where 3D surfaces of Actin and the mitochondria were created. The software computed the contact area between the two surfaces as well as colocalization XTension to quantify the colocalized voxels between the Drp1 surface and the mitochondrial surface.

Cell culture and generation of stable cell lines. SH-SY5Y cell lines were grown in DMEM/F12 medium (Gibco) supplemented with 10% (v/v) fetal calf serum (FCS; Thermo Scientific), 2 mM L-glutamine (Gibco), 1 x MEM non-essential amino acids, 100 U/ml penicillin and 100 μ g/ml streptomycin (Gibco) in a humidified incubator at 37 °C, 5% CO₂ and 95% air. The SH-SY5Y cell lines pLKO-NT (control) and G4 (knockdown) were a kind gift of David Pla-Martin and Francesc Palau¹⁹ and were grown in growth medium containing 2 μ g/ml puromycin (InvivoGen).

Measurement of mitochondrial oxygen consumption. Mitochondrial respiration and oxygen consumption were analyzed using the Oxygraph-2k (Oroboros Instruments). Cells in suspension at a density of 1.5–2.0 \times 10⁶ cells/ml were analyzed under continuous stirring at 750 rpm and 37 °C. All chemicals with the exception of palmitate-BSA were purchased from Sigma. Palmitate-BSA was purchased from Biomol. In a phosphorylation-control-protocol, the routine respiration of cells in their general growth medium was measured following the addition of 2 μ g/ml oligomycin to inhibit the ATP synthase and measure leak respiration. By titration of the protonophore carbonyl cyanide 4-(tri-fluoromethoxy) phenylhydrazone in 0.5 μ M steps the respiration was stimulated up to a maximum oxygen flow and the electron transfer system capacity was determined. By the addition of 0.5 μ M rotenone and 2.5 μ M antimycin A the respiration was inhibited and the non-mitochondrial residual oxygen consumption was measured. In 2 s intervals, the oxygen concentration and the oxygen flow per cells were recorded using the DatLab software 5.1 (Oroboros Instruments). All measurements were performed after daily calibration of the polarographic oxygen sensors and using instrumental background correction. The measured respiratory states were analyzed after correction with ROX to compare only mitochondrial oxygen consumption.

ATP measurements. Cytosolic and mitochondrial ATP levels were quantified as described²⁷. Cells were transiently transfected with plasmids carrying the bioluminescence energy transfer (BRET)-based ATP biosensor BTeam without targeting signal sequence (for cyto-ATP determination) or targeted to mitochondria (for mito-ATP determination) using TurboPectin reagent (OriGene). The plasmids were a kind gift of Hiroshi Imamura, University of Kyoto. 48 h later, the cells were incubated for 30 min in phenol red-free medium supplemented with 30 μ M NanoLuciferase (NLuc) inhibitor to avoid disturbance from the BTeam released from dead cells. Afterwards, NLuc substrate (Promega) was added to the medium and the plate incubated for 20 min. Subsequently, luminescent emissions from the cells were measured at 37 °C at 520/560 nm (Yellow Fluorescent Protein (YFP) emission) and at 430/470 nm (NLuc emission) using a Tecan Spark® Multimode Microplate Reader.

Glutamine and glutamate measurements. The glutamine-glutamate-glo assay (Promega, # J8021) was performed according to manufacturer's instructions to determine intracellular glutamine and glutamate concentrations. Briefly, 20,000 cells of the SH-SY5Y cell line and 100,000 motoneurons were plated in triplicates per experiment on white 96-well plates (Greiner, # 655083) two or seven days prior to the experiment, respectively. On the day of the experiment, cells were washed twice with PBS and 30 μ l of PBS as well as 15 μ l of 0.3 HCl solution was added to the cells and mixed for 5 min. 15 μ l of 450 mM Tris solution, pH 8.0 was added and incubated for further 60 sec. From each lysate, 25 μ l was transferred into a new white 96-well plate for I) glutamine plus glutamate and II) glutamate only measurement. Glutaminase was only added to the first set of wells and incubated for 30 min at RT. The detection reagent composed of Luciferin detection solution, reductase, reductase substrate, GLUD1 and NAD was added to all wells and incubated for 60 min at RT before luminescence detection in a Tecan Infinite 200 pro plate reader. Concentrations were calculated with glutamine and glutamate standard curves (0.78 to 50 μ M) and a blank was included to remove any assay background signal. Glutamate levels were calculated by subtracting the glutamate-only signal from the signal containing glutamate and glutamine levels together.

Electron microscopy and analysis. Cells were pelleted by centrifugation at 1300 rpm for 3 min and fixed in 3% glutaraldehyde overnight. Following several

rinses in 0.2 M sodium cacodylate buffer (pH 7.3), the samples were postfixed in 1% osmium tetroxide in cacodylate buffer for 2 h, dehydrated through an ascending series of ethanol concentrations and embedded in resin with propylene oxide as an intermediary. Semi-thin (0.65 μm) sections for light microscopy and ultrathin (50 nm) sections for electron microscopy were cut on a Leica Ultracut UCT ultramicrotome. Semi-thin sections were stained with methylene blue. Ultrathin sections were stained with an alcoholic solution of 1% uranyl acetate and lead citrate in sodium hydroxide and examined with a Zeiss EM-910 transmission electron microscope. For morphometric and quantitative analysis, representative cells were photographed at a magnification of 10,000 and 18,000. Analyses were done with ImageJ. MERCs were defined by a distance of mitochondrial and ER membranes between ~10 and ~50 nm. The frequency distribution of the MERCs width was calculated using GraphPad.

Biochemical analysis of mitochondria-ER contact sites. Cells were detached using trypsin/EDTA and resuspended in 1–2 ml of a buffer containing 0.32 M sucrose, 10 mM Tris-HCl, 1 mM EDTA and protease (Roche Diagnostics, 04693124001) and phosphatase (Roche Diagnostics, 04906845001) inhibitors. Cells were disrupted by a nitrogen decompression instrument (Parr Instrument Company, 4639) and centrifuged (2000 g, 10 min). The supernatant was transferred to a new microtube, centrifuged at 10,000 g for 10 min and the cell pellet resuspended in 1 ml of the same buffer containing the same components as above except 0.5 M sucrose. Finally, mitochondria were sedimented by centrifugation at 10,000 g for 10 min and resolved in an appropriate amount of RIPA buffer for the subsequent experiments.

FRET-based FEMP probe to quantify mitochondria-ER contact sites. MERCs were quantified with a FRET-based sensor indicating the proximity between the ER and mitochondria. The plasmid encodes for a YFP-linked outer mitochondrial membrane protein Akap1 and a CFP-conjugated ER-protein Sac1, as well as a fused FKBP and FRB domain respectively and is available from Marta Giacomello, University of Padova. These domains can form heterodimers upon rapamycin treatment. The specific localization of these proteins is ensured by the introduction of a self-cleavable Tav2A sequence^{34,35}. The FEMP plasmid (FRET-based ER-mitochondria probe) was transfected with GenJet. 48 h later, images were taken with the Perkin Elmer Operetta High-Content Imaging System acquiring the CFP- (410-430/460-500 ex/em), YFP- (490-510/520-560 ex/em) and YFP_{FRET}-emission (410-430/520-560 ex/em) with a $\times 40$ water objective for determination of the basal distances between the organelles. Subsequently, the cells were treated with 100 nM rapamycin for 15 min for FKBP-FRB dimerization induction and to reach a maximum of YFP_{FRET} signal. Cells were fixed for another 20 min with 1% PFA and imaging was performed again with equal microscopy settings. For the analysis, the Harmony software was used. First, the cells were identified using the YFP channel. Within each cell and region of interest (ROI), the intensities of the three acquired channels were calculated, including background subtraction. FRET basal and FRET max were calculated as: $(\text{FYFP-FRET}_{\text{cell}} - \text{FYFP-FRET}_{\text{background}}) / (\text{FCFP}_{\text{cell}} - \text{FCFP}_{\text{background}})$; FRET Ratio was calculated as $(\text{FRET}_{\text{max}} - \text{FRET}_{\text{basal}}) / \text{FRET}_{\text{basal}}$.

Mitochondrial Ca²⁺ measurement. Dye: Cells were plated (20,000 cells/cm²) in 8-well μ -slides ibiTreat (ibidi, 80826) and treated with 5 μM of Rhod2-AM (Molecular Probes, R1245MP) in culture medium without FBS for 60 min at 37 °C the next day. Rhod2-AM fluorescent signals were analyzed at (Ex/Em) 549/578 nm wavelengths using a Leica SP5 confocal microscope and analyzed by ImageJ. Genetically encoded reporter: Cells were transfected with the genetically encoded reporters and analyzed two days later in an inverted TCS-SP5 confocal microscope (Leica) with appropriate excitation/emission wavelengths as reported for CEPIA3mt (Addgene, 58219) and GEM-CEPIA1er (Addgene, 58217)³¹. The CEPIA3mt construct was co-transfected and normalized to mito-TurboFarRed.

Aequorin Ca²⁺ measurements. For Ca²⁺ measurements, the biosensor aequorin (AEQ) was used, which is a 22 kDa calcium-binding photoprotein isolated from jellyfish *Aequorea Victoria*. The plasmid is available from Marta Giacomello, University of Padova. SH-SY5Y cells were grown on 12 mm glass coverslips to a confluence of 40–50% and transfected with cytosolic or mitochondria-targeted AEQ (cytAEQ/mtAEQ) using GenJet. On the day of the experiment, the cells were treated with 5 μM coelenterazine-N-AM (Santa Cruz Biotechnology sc-205904) in basic saline solution (BS, 135 mM NaCl₂, 5 mM KCl, 0.4 mM KH₂PO₄, 1 mM MgSO₄ \times 7 H₂O, 20 mM HEPES, 0.1% (w/v) glucose, pH 7.4 adjustment at 37 °C with NaOH 10 N) containing 1 mM CaCl₂ for 2 h at 37 °C and 5% CO₂. Coelenterazine served as a substrate for AEQ. Cover slides were then placed in the luminometer with constant buffer perfusion with BS supplemented with I) 1 mM Ca²⁺ (30 s) II) 200 μM EGTA (30 s) III) 200 μM Carbachol (CCH) + 200 μM EGTA (120 s) IV) 100 μM Digitonin + 5 mM CaCl₂ (220 s).

Precipitation of biotinylated Avi-GDAP1. Primary cortical neuron cultures were prepared from embryos (E16) from the transgenic mouse line Gt(ROSA)26Sortm1(birA)Mejr (ROSA26-BirA) of a C57BL/6 N background. In this mouse strain, the biotin ligase BirA was inserted into the gene locus of the ROSA26 promoter⁴⁰. Cortical neurons were cultured on poly-D-lysine coated plates

(0.05 mg/ml) in Neurobasal medium (NBM, Life Technologies, 21103049) supplemented with 2% (v/v) B-27 supplement (Life Technologies, 17504-044), 1% (v/v) L-glutamine (Sigma-Aldrich, G1251) and 100 U/ml penicillin and 100 $\mu\text{g}/\text{ml}$ streptomycin (Sigma-Aldrich, P0781). Medium change was performed at day 1 and day 4 after isolation. For transduction of the primary neurons, viruses were added in a volume that equaled 6×10^7 – 8×10^7 copies/ μl per well of a 6 well plate containing 4 ml of NBM and neurons on day 4 after isolation. Neurons were cultured for further 7 days. Cells were harvested, washed with PBS and lysed in RIPA buffer supplemented with protease inhibitors. The samples were centrifuged at 21,000 g for 30 min at 4 °C, the proteins concentration was determined via BC-Assay and 20 μg protein lysate was removed as input-control. Protein lysates were either directly incubated with Dynabeads™ MyOne™ Streptavidin T1 according to the manufacturer's protocol or taken for GSH or GSSG incubation (5 mM GSH or GSSG in 10 mM HEPES pH 7.4, 35 mM sucrose, 40 mM KCl, 0.25 mM EGTA, 2 mM Mg(CH₃COO)₂, 0.5 mM GTP, 1 mM ATP (K⁺), 5 mM Na-succinate, 0.08 mM ADP, 2 mM K₂HPO₄ for 30 min at 37 °C). Dynabeads™ MyOne™ Streptavidin T1 were incubated for 45 min at RT on a shaker. Dynabeads were washed three times with RIPA buffer and once with PBS and stored at –80 °C until further processing for LC-MS.

Protein elution, lysis and digestion. Bound proteins were eluted from Dynabeads in 10 mM Tris pH 8.0, 2% SDS, 1 mM Biotin at 80 °C. Whole cells were lysed in 5 μl of 10% SDS at 95 °C for 5 min. Protein samples were digested using the SP3 (“Single-Pot Solid-Phase-Enhanced Sample Preparation”) protocol⁷⁴ with modifications⁷⁵. Proteins were reduced by adding 5 μl of 200 mM Dithiothreitol (DTT) per 100 μl lysate (45 °C, 30 min). Free cysteines were subsequently alkylated by adding 10 μl 100 mM Iodoacetamide (IAA) per 100 μl lysate (RT, 30 min, in the dark). Subsequently, remaining IAA was quenched by adding 10 μl 200 mM DTT per 100 μl lysate. Magnetic carboxylate modified particles Beads (SpeedBeads, Sigma) were used for protein clean-up and acetonitrile (ACN), in a final concentration of 70%, was added to the samples to induce the binding of the proteins to the beads by hydrophilic interactions (18 min RT). By incubating the bead-protein mixture on a magnetic stand for 2 min, the sample was bound to the magnet and the supernatant removed, followed by two washing steps with 70% ethanol (EtOH), addition of 180 μl ACN, incubation for 15 s and removal of the solvent. Finally, 5 μl digest buffer (50 mM ammonium bicarbonate, 1:25 w/w trypsin:protein ratio) was added to the air-dried bead-protein mixtures and incubated overnight at 37 °C. To purify peptides after digestion, ACN was added to a final concentration of 95%. After another washing step, the beads were resuspended in 10 μl 2% DMSO (in water), put into an ultrasonic bath for 1 min and then shortly centrifuged. 10 μl of the resulting supernatant was mixed with 5 μl 100 fmol/ μl Enolase digest (Waters Corporation) and acidified with 5 μl 1% formic acid (FA).

LC-MS analysis. Liquid chromatography (LC) of tryptic peptides was performed on a NanoAQUITY UPLC system (Waters Corporation) equipped with 75 μm \times 250 mm HSS-T3 C18 column (Waters corporation). Mobile phase A was 0.1% (v/v) formic acid (FA) and 3% (v/v) DMSO in water. Mobile phase B was 0.1% (v/v) FA and 3% (v/v) DMSO in ACN. Peptides were separated running a gradient from 5 to 40% (v/v) mobile phase B at a flow rate of 300 nL/min over 90 min. The column was heated to 55 °C. MS analysis of eluting peptides was performed by ion-mobility enhanced data-independent acquisition (UDMS^E). Precursor ion information was collected in low-energy MS mode at a constant collision energy of 4 eV. Fragment ion information was obtained in the elevated energy scan applying drift-time specific collision energies. The spectral acquisition time in each mode was 0.7 s with a 0.05 s interscan delay resulting in an overall cycle time of 1.5 s for the acquisition of one cycle of low and elevated energy data. [Glu1]-fibrinopeptide was used as lock mass at 100 fmol/ μL and sampled every 30 s into the mass spectrometer via the reference sprayer of the NanoLockSpray source. All samples were analyzed in three technical replicates.

Data processing and label-free protein quantification. UDMS^E data processing and database search was performed using ProteinLynx Global Server (PLGS, ver. 3.0.2, Waters Corporation). The resulting proteins were searched against the UniProt proteome database (species: *Mus musculus*, UniProtK-Swissprot release 2019_05, 17,051 entries; *Homo sapiens*, UniProtK-Swissprot release 2019_10, 20367 entries) supplemented with a list of common contaminants. The database search was specified by trypsin as enzyme for digestion and peptides with up to two missed cleavages were included. Carbamidomethyl cysteine was set as fixed modification and oxidized methionine as variable modification. False discovery rate assessment for peptide and protein identification was done using the target-decoy strategy by searching a reverse database and was set to 0.01 for database search in PLGS. Retention time alignment, exact mass retention time (EMRT), as well as normalization and filtering were performed in ISOQuant ver.1.8. By using TOP3 quantification, absolute in-sample amounts of proteins were calculated.

Statistics and reproducibility. Normal distribution was tested using the D'Agostino-Pearson omnibus normality test. Statistical significance was then verified using appropriate parametric (Student's *t* test or ANOVA) or non-parametric

tests (Mann–Whitney and Kruskal–Wallis tests) followed by multiple comparison tests as indicated. The Wilcoxon signed rank test was used when normalization to 100% was necessary as indicated. Statistical analysis of mass spectrometry data was performed using two-tailed, paired t-tests and subsequent Bonferroni correction. Here, a corrected $p < 0.01$ was considered significant for the biotinylated Avi-GDAP1 pulldown experiment and $p < 0.05$ for whole cell lysates. In all other data a $p < 0.05$ was considered to be statistically significant. Pathway over-representation analysis was performed using the STRING database with default parameters³⁹. KEGG pathway visualization was performed using the R package clusterProfiler⁷⁶.

Reporting summary. Further information on research design is available in the Nature Research Reporting Summary linked to this article.

Data availability

The mass spectrometry proteomics data have been deposited to the ProteomeXchange Consortium (<http://proteomecentral.proteomexchange.org>) via the PRIDE partner repository⁷⁷ with the data set identifiers: <PXD024555> for the biotinylated Avi-GDAP1 coprecipitation experiment; and <PXD028460> for the GDAP1 KD label-free quantification experiment. Plasmids used are mentioned in the Methods section and can be requested from those that generated them upon reasonable request. Supplementary Data 1 contains all raw data and uncropped immunoblots.

Received: 24 March 2022; Accepted: 11 May 2022;

Published online: 03 June 2022

References

- Baxter, R. V. et al. Ganglioside-induced differentiation-associated protein-1 is mutant in Charcot-Marie-Tooth disease type 4A/8q21. *Nat. Genet.* **30**, 21–22 (2002).
- Cuesta, A. et al. The gene encoding ganglioside-induced differentiation-associated protein 1 is mutated in axonal Charcot-Marie-Tooth type 4A disease. *Nat. Genet.* **30**, 22–25 (2002).
- Senderek, J. et al. Mutations in the ganglioside-induced differentiation-associated protein-1 (GDAP1) gene in intermediate type autosomal recessive Charcot-Marie-Tooth neuropathy. *Brain* **126**, 642–649 (2003).
- Chung, K. W. et al. A novel GDAP1 Q218E mutation in autosomal dominant Charcot-Marie-Tooth disease. *J. Hum. Genet.* **53**, 360–364 (2008).
- Marco, A., Cuesta, A., Pedrola, L., Palau, F. & Marin, I. Evolutionary and structural analyses of GDAP1, involved in Charcot-Marie-Tooth disease, characterize a novel class of glutathione transferase-related genes. *Mol. Biol. Evol.* **21**, 176–187 (2004).
- Shield, A. J., Murray, T. P. & Board, P. G. Functional characterisation of ganglioside-induced differentiation-associated protein 1 as a glutathione transferase. *Biochem. Biophys. Res. Commun.* **347**, 859–866 (2006).
- Wagner, K. M., Rüegg, M., Niemann, A. & Suter, U. Targeting and function of the mitochondrial fission factor GDAP1 are dependent on its tail-anchor. *PLoS ONE* **4**, e5160 (2009).
- Pedrola, L. et al. GDAP1, the protein causing Charcot-Marie-Tooth disease type 4A, is expressed in neurons and is associated with mitochondria. *Hum. Mol. Genet.* **14**, 1087–1094 (2005).
- Huber, N. et al. Glutathione-conjugating and membrane-remodeling activity of GDAP1 relies on amphipathic C-terminal domain. *Sci. Rep.* **6**, 36930 (2016).
- Googins, M. R. et al. Structural and functional divergence of GDAP1 from the glutathione S-transferase superfamily. *FASEB J.* **34**, 7192–7207 (2020).
- Niemann, A., Ruegg, M., La Padula, V., Schenone, A. & Suter, U. Ganglioside-induced differentiation associated protein 1 is a regulator of the mitochondrial network: new implications for Charcot-Marie-Tooth disease. *J. Cell Biol.* **170**, 1067–1078 (2005).
- Huber, N., Guimaraes, S., Schrader, M., Suter, U. & Niemann, A. Charcot-Marie-Tooth disease-associated mutants of GDAP1 dissociate its roles in peroxisomal and mitochondrial fission. *EMBO Rep.* **14**, 545–552 (2013).
- Niemann, A., Wagner, K. M., Ruegg, M. & Suter, U. GDAP1 mutations differ in their effects on mitochondrial dynamics and apoptosis depending on the mode of inheritance. *Neurobiol. Dis.* **36**, 509–520 (2009).
- Ingerman, E. et al. Dnm1 forms spirals that are structurally tailored to fit mitochondria. *J. Cell Biol.* **170**, 1021–1027 (2005).
- Friedman, J. R. et al. ER tubules mark sites of mitochondrial division. *Science* **334**, 358–362 (2011).
- De Vos, K. J., Allan, V. J., Grierson, A. J. & Sheetz, M. P. Mitochondrial function and actin regulate dynamin-related protein 1-dependent mitochondrial fission. *Curr. Biol.* **15**, 678–683 (2005).
- Korobova, F., Ramabhadran, V. & Higgs, H. N. An actin-dependent step in mitochondrial fission mediated by the ER-associated formin INF2. *Science* **339**, 464–467 (2013).
- Chakrabarti, R. et al. INF2-mediated actin polymerization at the ER stimulates mitochondrial calcium uptake, inner membrane constriction, and division. *J. Cell Biol.* **217**, 251–268 (2018).
- Pla-Martín, D. et al. Silencing of the Charcot-Marie-Tooth disease-associated gene GDAP1 induces abnormal mitochondrial distribution and affects Ca²⁺ homeostasis by reducing store-operated Ca²⁺ entry. *Neurobiol. Dis.* **55**, 140–151 (2013).
- Boyer, O. et al. INF2 mutations in Charcot-Marie-Tooth disease with glomerulopathy. *N. Engl. J. Med.* **365**, 2377–2388 (2011).
- Rehklau, K. et al. Cofilin1-dependent actin dynamics control DRP1-mediated mitochondrial fission. *Cell Death Dis.* **8**, e3063 (2017).
- González-Sánchez, P. et al. CMT-linked loss-of-function mutations in GDAP1 impair store-operated Ca²⁺ entry-stimulated respiration. *Sci. Rep.* **7**, 42993 (2017).
- Chance, B. The energy-linked reaction of calcium with mitochondria. *J. Biol. Chem.* **240**, 2729–2748 (1965).
- Kennerson, M. L. et al. A new locus for X-linked dominant Charcot-Marie-Tooth disease (CMTX6) is caused by mutations in the pyruvate dehydrogenase kinase isoenzyme 3 (PDK3) gene. *Hum. Mol. Genet.* **22**, 1404–1416 (2013).
- Pla-Martín, D. et al. Junctophilin-1 is a modifier gene of GDAP1-related Charcot-Marie-Tooth disease. *Hum. Mol. Genet.* **24**, 213–229 (2015).
- Noack, R. et al. Charcot-Marie-Tooth disease CMT4A: GDAP1 increases cellular glutathione and the mitochondrial membrane potential. *Hum. Mol. Genet.* **21**, 150–162 (2012).
- Yoshida, T., Kakizuka, A. & Imamura, H. BTeam, a novel BRET-based biosensor for the accurate quantification of ATP concentration within living cells. *Sci. Rep.* **6**, 39618 (2016).
- Denton, R. M., Randle, P. J. & Martin, B. R. Stimulation by calcium ions of pyruvate dehydrogenase phosphate phosphatase. *Biochem. J.* **128**, 161–163 (1972).
- Denton, R. M., Richards, D. A. & Chin, J. G. Calcium ions and the regulation of NAD⁺-linked isocitrate dehydrogenase from the mitochondria of rat heart and other tissues. *Biochem. J.* **176**, 899–906 (1978).
- Zhao, Y. et al. Site-directed mutagenesis of phosphorylation sites of the branched chain alpha-ketoacid dehydrogenase complex. *J. Biol. Chem.* **269**, 18583–18587 (1994).
- Suzuki, J. et al. Imaging intraorganellar Ca²⁺ at subcellular resolution using CEPIA. *Nat. Commun.* **5**, 4153 (2014).
- Giacomello, M. & Pellegrini, L. The coming of age of the mitochondria-ER contact: a matter of thickness. *Cell Death Differ.* **23**, 1417–1427 (2016).
- Marchi, S., Patergnani, S. & Pinton, P. The endoplasmic reticulum-mitochondria connection: one touch, multiple functions. *Biochim. Biophys. Acta* **1837**, 461–469 (2014).
- Csordás, G. et al. Imaging interorganelle contacts and local calcium dynamics at the ER-mitochondrial interface. *Mol. Cell* **39**, 121–132 (2010).
- Naon, D. et al. Critical reappraisal confirms that Mitofusin 2 is an endoplasmic reticulum-mitochondria tether. *Proc. Natl Acad. Sci. USA* **113**, 11249–11254 (2016).
- Giacomello, M. et al. Ca²⁺ hot spots on the mitochondrial surface are generated by Ca²⁺ mobilization from stores, but not by activation of store-operated Ca²⁺ channels. *Mol. Cell* **38**, 280–290 (2010).
- Szabadkai, G. et al. Chaperone-mediated coupling of endoplasmic reticulum and mitochondrial Ca²⁺ channels. *J. Cell Biol.* **175**, 901–911 (2006).
- Tenzen, S. et al. Proteome-wide characterization of the RNA-binding protein RALY-interactome using the in vivo-biotinylation-pulldown-quant (iBioPQ) approach. *J. Proteome Res.* **12**, 2869–2884 (2013).
- Szklarczyk, D. et al. The STRING database in 2021: customizable protein-protein networks, and functional characterization of user-uploaded gene/measurement sets. *Nucleic Acids Res.* **49**, D605–D612 (2020).
- Driegen, S. et al. A generic tool for biotinylation of tagged proteins in transgenic mice. *Transgenic Res.* **14**, 477–482 (2005).
- Cull, M. G. & Schatz, P. J. Biotinylation of proteins in vivo and in vitro using small peptide tags. *Methods Enzymol.* **326**, 430–440 (2000).
- Shutt, T., Geoffroy, M., Milne, R. & McBride, H. M. The intracellular redox state is a core determinant of mitochondrial fusion. *EMBO Rep.* **13**, 909–915 (2012).
- Bittermann, E. et al. Differential requirements of tubulin genes in mammalian forebrain development. *PLoS Genet.* **15**, e1008243 (2019).
- Estela, A., Pla-Martín, D., Sánchez-Piris, M., Sesaki, H. & Palau, F. Charcot-Marie-Tooth-related gene GDAP1 complements cell cycle delay at G2/M phase in *Saccharomyces cerevisiae* fis1 gene-defective cells. *J. Biol. Chem.* **286**, 36777–36786 (2011).
- Klemke, M. et al. Oxidation of cofilin mediates T cell hyporesponsiveness under oxidative stress conditions. *Immunity* **29**, 404–413 (2008).

46. Gellert, M., Hanschmann, E.-M., Lepka, K., Berndt, C. & Lillig, C. H. Redox regulation of cytoskeletal dynamics during differentiation and de-differentiation. *Biochim. Biophys. Acta* **1850**, 1575–1587 (2015).
47. Kruyer, A., Ball, L. E., Townsend, D. M., Kalivas, P. W. & Uys, J. D. Post-translational S-glutathionylation of cofilin increases actin cycling during cocaine seeking. *PLoS ONE* **14**, e0223037 (2019).
48. Melak, M., Plessner, M. & Grosse, R. Actin visualization at a glance. *J. Cell Sci.* **130**, 525–530 (2017).
49. Bunnell, T. M., Burbach, B. J., Shimizu, Y. & Ervasti, J. M. β -Actin specifically controls cell growth, migration, and the G-actin pool. *Mol. Biol. Cell* **22**, 4047–4058 (2011).
50. McGough, A., Pope, B., Chiu, W. & Weeds, A. Cofilin changes the twist of F-actin: implications for actin filament dynamics and cellular function. *J. Cell Biol.* **138**, 771–781 (1997).
51. Ji, W.-K., Hatch, A. L., Merrill, R. A., Strack, S. & Higgs, H. N. Actin filaments target the oligomeric maturation of the dynamin GTPase Drp1 to mitochondrial fission sites. *Elife* **4**, e11553 (2015).
52. Patron, M. et al. MICU1 and MICU2 finely tune the mitochondrial Ca^{2+} uniporter by exerting opposite effects on MCU activity. *Mol. Cell* **53**, 726–737 (2014).
53. Civera-Tregón, A. et al. Mitochondria and calcium defects correlate with axonal dysfunction in GDAP1-related Charcot-Marie-Tooth mouse model. *Neurobiol. Dis.* **152**, 105300 (2021).
54. Boldogh, I. R. & Pon, L. A. Interactions of mitochondria with the actin cytoskeleton. *Biochim. Biophys. Acta* **1763**, 450–462 (2006).
55. Hoffmann, L. et al. Cofilin1 oxidation links oxidative distress to mitochondrial demise and neuronal cell death. *Cell Death Dis.* **12**, 953 (2021).
56. Pope, B. J., Zierler-Gould, K. M., Kühne, R., Weeds, A. G. & Ball, L. J. Solution structure of human cofilin: actin binding, pH sensitivity, and relationship to actin-depolymerizing factor. *J. Biol. Chem.* **279**, 4840–4848 (2004).
57. Pfannstiel, J. et al. Human cofilin forms oligomers exhibiting actin bundling activity. *J. Biol. Chem.* **276**, 49476–49484 (2001).
58. Goyal, P. et al. Cofilin oligomer formation occurs in vivo and is regulated by cofilin phosphorylation. *PLoS ONE* **8**, e71769 (2013).
59. Siudeja, K., Grzeschik, N. A., Rana, A., de Jong, J. & Sibon, O. C. M. Cofilin/Twinstar phosphorylation levels increase in response to impaired coenzyme A metabolism. *PLoS ONE* **7**, e43145 (2012).
60. Chua, B. T. et al. Mitochondrial translocation of cofilin is an early step in apoptosis induction. *Nat. Cell Biol.* **5**, 1083–1089 (2003).
61. Klamt, F. et al. Oxidant-induced apoptosis is mediated by oxidation of the actin-regulatory protein cofilin. *Nat. Cell Biol.* **11**, 1241–1246 (2009).
62. Luo, S., Uehara, H. & Shacter, E. Taurine chloramine-induced inactivation of cofilin protein through methionine oxidation. *Free Radic. Biol. Med.* **75**, 84–94 (2014).
63. Fratelli, M. et al. Identification by redox proteomics of glutathionylated proteins in oxidatively stressed human T lymphocytes. *Proc. Natl Acad. Sci. USA* **99**, 3505–3510 (2002).
64. Orth, J. D., Krueger, E. W., Cao, H. & McNiven, M. A. The large GTPase dynamin regulates actin comet formation and movement in living cells. *Proc. Natl Acad. Sci. USA* **99**, 167–172 (2002).
65. Lee, E. & De Camilli, P. Dynamin at actin tails. *Proc. Natl Acad. Sci. USA* **99**, 161–166 (2002).
66. Züchner, S. et al. Mutations in the pleckstrin homology domain of dynamin 2 cause dominant intermediate Charcot-Marie-Tooth disease. *Nat. Genet.* **37**, 289–294 (2005).
67. Fabrizi, G. M. et al. Two novel mutations in dynamin-2 cause axonal Charcot-Marie-Tooth disease. *Neurology* **69**, 291–295 (2007).
68. Lee, J. E., Westrate, L. M., Wu, H., Page, C. & Voeltz, G. K. Multiple dynamin family members collaborate to drive mitochondrial division. *Nature* **540**, 139–143 (2016).
69. Luigetti, M. et al. Seipin S90L mutation in an Italian family with CMT2/dHMN and pyramidal signs. *Muscle Nerve* **42**, 448–451 (2010).
70. Boutet, E. et al. Seipin deficiency alters fatty acid Delta9 desaturation and lipid droplet formation in Berardinelli-Seip congenital lipodystrophy. *Biochimie* **91**, 796–803 (2009).
71. Tian, Y. et al. Tissue-autonomous function of Drosophila seipin in preventing ectopic lipid droplet formation. *PLoS Genet.* **7**, e1001364 (2011).
72. Yang, W. et al. BSCL2/seipin regulates adipogenesis through actin cytoskeleton remodeling. *Hum. Mol. Genet.* **23**, 502–513 (2014).
73. Reinhardt, P. et al. Derivation and expansion using only small molecules of human neural progenitors for neurodegenerative disease modeling. *PLoS ONE* **8**, e59252 (2013).
74. Hughes, C. S. et al. Ultrasensitive proteome analysis using paramagnetic bead technology. *Mol. Syst. Biol.* **10**, 757 (2014).
75. Sielaff, M. et al. Evaluation of FASP, SP3, and iST Protocols for Proteomic Sample Preparation in the Low Microgram Range. *J. Proteome Res.* **16**, 4060–4072 (2017).
76. Wu, T. et al. clusterProfiler 4.0: A universal enrichment tool for interpreting omics data. *Innov. J.* **2**, 100141 (2021).
77. Vizcaino, J. A. et al. The PRoteomics IDentifications (PRIDE) database and associated tools: status in 2013. *Nucleic Acids Res.* **41**, D1063–D1069 (2013).

Acknowledgements

The excellent support by the IMB Core Facility Microscopy is gratefully acknowledged. This work was supported by grants of the Deutsche Forschungsgemeinschaft to A.M. (CRC1080 project A10) and to A.M. and E.M.H. and S.T. (DFG ME1922 16-1; Ha 8334/2-2; TE599/6-1) within the priority program 1710. This work was supported by an Excellence Grant of the Luxembourg National Research Fund (FNR) within the PEARL program (FNR; FNR/P13/6682797 to R.K.). Work of R.K. is further supported by a grant from the FNR within the National Centre of Excellence in Research on Parkinson's disease (NCER-PD). We thank the Disease Modelling and Screening Platform of the Luxembourg Institute of Systems Biomedicine and the Luxembourg Institute of Health for their support on high-content imaging of motoneurons. We thank Marion Silies for excellent and exhaustive proofreading.

Author contributions

C.W., A.P., S.B., AnnP, D.B., P.M., F.d.B., C.V., I.B., D.G., P.M. carried out experiments; K.D., M.P., and O.B. generated the iPS cells; J.S. and S.R. helped establishing high-content microscopy; S.A., D.G., and S.T. analyzed quantitative proteomic analyses; M.G. supervised and analyzed the FEMP and aequorin measurements; R.K. supervised and analyzed the experiments with human motoneurons; C.W., M.S., and E.M.H. analyzed data and helped writing the manuscript; A.M. devised experiments, analyzed data and wrote the manuscript.

Funding

Open Access funding enabled and organized by Projekt DEAL.

Competing interests

The authors declare no competing interests.

Additional information

Supplementary information The online version contains supplementary material available at <https://doi.org/10.1038/s42003-022-03487-6>.

Correspondence and requests for materials should be addressed to Axel Methner.

Peer review information This manuscript has been previously reviewed at another Nature Portfolio journal. The manuscript was considered suitable for publication without further review at *Communications Biology*. Primary Handling Editors: Eve Rogers.

Reprints and permission information is available at <http://www.nature.com/reprints>

Publisher's note Springer Nature remains neutral with regard to jurisdictional claims in published maps and institutional affiliations.



Open Access This article is licensed under a Creative Commons Attribution 4.0 International License, which permits use, sharing, adaptation, distribution and reproduction in any medium or format, as long as you give appropriate credit to the original author(s) and the source, provide a link to the Creative Commons license, and indicate if changes were made. The images or other third party material in this article are included in the article's Creative Commons license, unless indicated otherwise in a credit line to the material. If material is not included in the article's Creative Commons license and your intended use is not permitted by statutory regulation or exceeds the permitted use, you will need to obtain permission directly from the copyright holder. To view a copy of this license, visit <http://creativecommons.org/licenses/by/4.0/>.

© The Author(s) 2022